



## Fast Au-Ni@ZIF-8-catalyzed ammonia borane hydrolysis boosted by dramatic volcano-type synergy and plasmonic acceleration



Naixin Kang<sup>a</sup>, Xiaorong Wei<sup>b</sup>, Ruofan Shen<sup>c</sup>, Baojun Li<sup>c,\*</sup>, Eduardo Guisasola Cal<sup>d</sup>, Sergio Moya<sup>d</sup>, Lionel Salmon<sup>e</sup>, Changlong Wang<sup>f</sup>, Emerson Coy<sup>g</sup>, Murielle Berlande<sup>a</sup>, Jean-Luc Pozzo<sup>a,\*</sup>, Didier Astruc<sup>a,\*</sup>

<sup>a</sup> ISM, UMR CNRS N° 5255, Univ. Bordeaux, 33405 Talence Cedex, France

<sup>b</sup> School of Environment and Energy, South China University of Technology, Guangzhou 510006, PR China

<sup>c</sup> Research Center of Green Catalysis, College of Chemistry, Zhengzhou University, 100 Science Road, Zhengzhou 450001, PR China

<sup>d</sup> Soft Matter Nanotechnology Lab, CIC biomaGUNE, Paseo Miramón 182, 20014 Donostia-San Sebastián, Gipuzkoa, Spain

<sup>e</sup> LCC, CNRS & University of Toulouse, 31077 Toulouse Cedex, France

<sup>f</sup> Institute of Circular Economy, Faculty of Materials and Manufacturing, Beijing University of Technology, Beijing 100124, PR China

<sup>g</sup> NanoBioMedical Centre, Adam Mickiewicz University, 61-614 Poznań, Poland

### ARTICLE INFO

#### Keywords:

Hydrogen production  
Ammonia borane hydrolysis  
Gold nanoalloy  
Volcano-type effect  
Plasmonic acceleration

### ABSTRACT

Production of hydrogen ( $H_2$ ) from  $H_2$  storage materials is very attractive as a source of sustainable energy. We report that AuNi@ZIF-8 alloys are very efficient nanocatalysts for  $H_2$  evolution upon ammonia borane hydrolysis under visible-light illumination with turnover frequency 3.4 times higher than with the monometallic Ni catalyst in the dark. This improvement is attributed to dramatic volcano-type positive synergy optimized in  $Au_{0.5}Ni_{0.5}$ @ZIF-8, for which ZIF-8 is by far the superior support, as well as to the localized surface plasmon resonance induced between 450 and 620 nm. Infrared spectra analysis and tandem reaction confirm the origin of the hydrogen atoms, reveal the reaction mechanism, and suggest how the cleavage of the B-H and O-H bonds proceeds in this reaction. Deuteration experiments with  $D_2O$  including primary kinetic isotope effects and density functional theory calculation under both dark and visible light conditions show that activation of  $H_2O$  always is the rate-determining step.

### 1. Introduction

Hydrogen ( $H_2$ ) has attracted wide attention as an extremely promising source of sustainable energy [1–3], but the challenge of storage and delivery of  $H_2$  limits its development [4–6]. Hydrogen-storage materials, such as boranes that are stable, high-hydrogen capacity, non-toxic, and water soluble [7], might prove useful both as energy sources and  $H_2$  reservoirs at the laboratory scale if a stimulus such as hydrolysis could rapidly and conveniently generate  $H_2$  from the precursor [8,9]. Many studies have demonstrated that metal nanoparticles (NPs) are effective catalysts for  $H_2$  evolution upon hydrolysis of ammonia borane (AB) according to Eq. 1[10–15].



Bimetallic catalysts are often particularly efficient because of the

possible synergies between the two metals forming the NPs [16–22]. For instance, Wang et al. compared the catalytic activity between Ni NPs and CuNi alloy for hydrogen production from AB and found that the activity was significantly enhanced by alloying Ni with Cu atoms, which was attributed to the change of local charge density due to Cu-Ni interactions [23]. Photocatalysis, a useful means of accelerating reactions, has been applied using plasmonic and semiconductors to  $H_2$  evolution from AB hydrolysis. Plasmon-induced visible light enhancement of AB hydrolysis rate, particularly with nanogold, also attracted the concern of scientists [24–27]. Indeed, the coinage metals Au, Ag and Cu have been widely studied because of their visible-light plasmonic response [28,29]. Rej's group reported visible-light accelerated AB hydrolysis catalyzed by core-shell AuPd NPs and theoretical calculations showing the presence of a special plasmonic resonance mode at the interphase of the catalyst [24]. Yamashita's group reported rate enhancement upon visible-light irradiation for  $H_2$  generation from AB catalyzed by Santa Barbara

\* Corresponding authors.

E-mail addresses: [lbjfcl@zju.edu.cn](mailto:lbjfcl@zju.edu.cn) (B. Li), [jean-luc.pozzo@u-bordeaux.fr](mailto:jean-luc.pozzo@u-bordeaux.fr) (J.-L. Pozzo), [didier.astruc@u-bordeaux.fr](mailto:didier.astruc@u-bordeaux.fr) (D. Astruc).

Amorphous (SBA)-15-stabilized Pt-Ag NPs [25]. Concerning heterogeneous catalysts, if the support is a good conductor, light enhancement due to the Mott-Schottky effect with the help of separated photo-generated electrons from a semiconductor between metal NPs and the semiconductor needs to be considered. Wang's group reported that the catalyst CuNi/CNS accelerates AB hydrolysis upon visible light irradiation, one of the favorable factors being the Mott-Schottky junctions between CuNi and CNS [23]. It was found earlier that ZIF-8 was an excellent support of Ni [14] and Ni<sub>2</sub>Pt [30] nanocatalysts for AB hydrolysis because of its ease and greenness of synthesis in aqueous solutions and very high thermal and chemical stabilities. However, the effect of visible light irradiation on catalysis by metal NPs supported by ZIF-8 has never been considered.

Therefore, we designed a new strategy involving both maximum synergy among the nanocomponents and plasmon-induced visible-light boosting catalytic AB hydrolysis performances. We fabricated such novel efficient alloyed nanomaterials consisting in ZIF-8-encapsulated Au-Ni catalysts for fast H<sub>2</sub> release from AB hydrolysis, and the results that are reported herein represent a great improvement with significant practical relevance [16,17]. Optimized cumulative effects of volcano-type positive synergy between nanogold and nickel, selective plasmonic visible-light excitation, and high selectivity and superiority of the ZIF-8 heterogeneous support are shown herein for nanocatalysis of AB hydrolysis by Ni-Au@ZIF-8. Any Mott-Schottky effect is shown to be discarded in this system. Kinetic isotope effects (KIEs) are used for the mechanistic study of this reaction, allowing the proposition of a viable hydrolysis mechanism. The efficiency of the best catalyst is also probed for a tandem hydrogenation reaction. Finally, Density functional theory (DFT) calculation on this process has been conducted to evaluate, together with the kinetic analysis, details of the reaction mechanism, and particular the rate-determining step (RDS) of this Ni-Au@ZIF-8-catalyzed AB hydrolysis in water under both dark and visible-light illumination conditions.

## 2. Materials and methods

### 2.1. Materials

Potassium gold chloride, nickel chloride, cobalt chloride, ferrous chloride, copper sulfate, sodium borohydride, AB, 2-methylimidazole, zinc nitrate hexahydrate and SBA-15 were purchased from Sigma-Aldrich. All flasks were washed with aqua regia (HCl: HNO<sub>3</sub> = 3:1) prior to use. All solutions and reagents were prepared using ultrapure water from the Barnstead Nano water purification system (Thermo Fisher Scientific Inc., USA).

### 2.2. Catalyst preparation

The synthesis of ZIF-8 was carried out according to a previous report [14]. Specifically, 2-methylimidazole (0.28 mol, 22.95 g) was dissolved in 80 mL water and stirred at room temperature to form a homogeneous solution. Then, an aqueous solution of zinc nitrate hexahydrate (1.19 g, 4.0 × 10<sup>-3</sup> mol) dissolved in 9 mL water was rapidly injected into the above aqueous solution. The mixture was stirred for 1 h, and the product was collected by centrifugation and washed 3 times with water. The obtained solid was then dried at 60 °C in vacuo overnight, and the white solids were collected for further use. Graphene oxide (GO) was prepared according to Hummers' method [31]. Biochar was obtained from the calcination of coffee husks as reported in the literature [32]. For the preparation of the nanocatalysts, generally, 100 mg ZIF-8 NPs dispersed in 5 mL water were injected into a 50 mL Schlenk flask under argon. The compositions of the Au-Ni alloyed NPs were adjusted by varying the molar ratios of the precursors. This mixture was stirred continuously at room temperature for 2 h, then degassed with nitrogen for 10 min. After degassing this solution, a 1-mL aqueous solution of freshly prepared NaBH<sub>4</sub> (10 equiv. per metal) was quickly added. The mixture was

further stirred for another 30 min, and the resulting nanocatalyst was collected by centrifugation and washed with deoxygenated water. Then, it was dried at 60 °C in vacuo overnight. The metal content of the nanocatalysts was quantified by inductively coupled plasma atomic emission spectroscopy (ICP-AES). For the synthesis of AuMNPs@ZIF-8 and AuNiNPs stabilized by another supports (GO, SBA-15, biochar), the steps were similar to those used for the synthesis of AuNi@ZIF-8 (see SI). For characterization methods and parameters, see SI.

### 2.3. Catalysis of the hydrolytic dehydrogenation of AB by AuNi@ZIF-8 in the dark

Under dark reaction conditions, the hydrolysis of AB was conducted in a 50-mL Schlenk flask at 25 ± 0.2 °C. Specifically, 50 mg of the catalyst AuNi@ZIF-8 was added to a flask with 4 mL water, then 1 mL of the aqueous solution of AB was added to the solution. The reaction time and determination of the volume of H<sub>2</sub> produced began when the AB solution was imported by a needle. In the standard treatment, the content of AuNi@ZIF-8 was 2.5% mmol, corresponding to a loading amount of AuNiNPs of 6.9%wt. The ratio between Au and the second metal (Fe, Co, Ni or Cu) was 1 to 1, and the amount of AB was 1 mmol.

### 2.4. Catalysis of hydrolytic dehydrogenation of AB by AuNi@ZIF-8 under visible-light irradiation

The photocatalytic reactions were performed by using 7-W visible LED strips (Sunshine Lighting Limited, France) at a light intensity of 1540 lx (each) with 520 nm light. The LED lamps were turned on for 15 min prior to irradiation to guarantee a stable light intensity. All the reactions under visible light were conducted with condensate circulation in order to keep the temperature at 25 ± 0.2 °C. The thermometer was placed inside the reaction cell. The dosage of catalyst and AB concentration were the same as in dark reactions, and the other steps were also kept the same as for the reactions under dark.

### 2.5. Hydrogenation of styrene catalyzed by AuNi@ZIF-8 using AB hydrolysis as the H<sub>2</sub> source

A sealed two-chamber device with two stirring bars was prepared. AB (1.0 mmol, 30.87 mg) and Au<sub>0.5</sub>Ni<sub>0.5</sub>@ZIF-8 (50 mg, 2.5% mmol per AB) were added into the left tube; the nanocatalyst Au<sub>0.5</sub>Ni<sub>0.5</sub>@ZIF-8 (20 mg, 1 mmol% per mmol styrene) and styrene (0.5 mmol, 52 mg) in 2 mL CD<sub>3</sub>OD were added into the right tube. After removing air in vacuo, the system was settled in an oil bath at 50 °C, and the mixture was stirred for 12 h. Then, the reaction solution in the right tube was collected by filtration for <sup>1</sup>H NMR and GC-MS analysis without any further treatment.

### 2.6. DFT calculations

The DFT methods are known to furnish an acceptable compromise between accuracy and applicability in large cell systems. Therefore, the ZIF-8 models have been simplified for ZIF-8 complex structures. Ni@ZIF-8, Au@ZIF-8 and AuNi@ZIF-8 have been established with the simplified ZIF-8 and metal cluster containing 38 atoms (Ni cluster, Au cluster and alloyed AuNi models). All spin-polarized calculations based on density functional theory (DFT) were performed utilizing DMol3 package [33]. The generalized gradient approximation (GGA) in the Perdew-Burke-Ernzerhof form and Semicore Pseudopotential method (DSPP) with the double numerical basis sets plus the polarization functional (DNP) were adopted [34]. The electronic properties, including density of states, electron density, orbitals and population analysis, in dye free form, have been studied. The double numerical basis set DNP has been used to predict dye electronic properties. In order to simplify the calculation, it has been considered that under the condition of illumination, the electrons of the structure are excited.

Therefore, the excited state for structure has been adopted to simulate the light effect. The photon energy of the wavelength of light used in the experiment is sufficient to reach the first excited states of Ni and Au. Thus, the Singlet option with 1st excited state has been chosen (operating options, Fig. S1). In addition, a DFT-D correction with Grimme scheme was used to account for the dispersion interaction [35]. The SCF convergence for each electronic energy was set as  $1.0 \times 10^{-5}$  Ha, and the

geometry optimization convergence criteria were set up as follows:  $1.0 \times 10^{-5}$  Ha for energy,  $0.001$  Ha  $\text{\AA}^{-1}$  for force, and  $0.01$   $\text{\AA}$  for displacement, respectively. Energy barriers were examined by linear and quadratic synchronous transit methods in combination with the conjugated gradient (CG) refinement. The free energies were obtained by  $G = E_{\text{total}} + E_{\text{ZPE}} - TS$ , where  $E_{\text{total}}$ ,  $E_{\text{ZPE}}$  and  $TS$  are the ground-state energy, zero-point energies, and entropy terms, respectively, with the

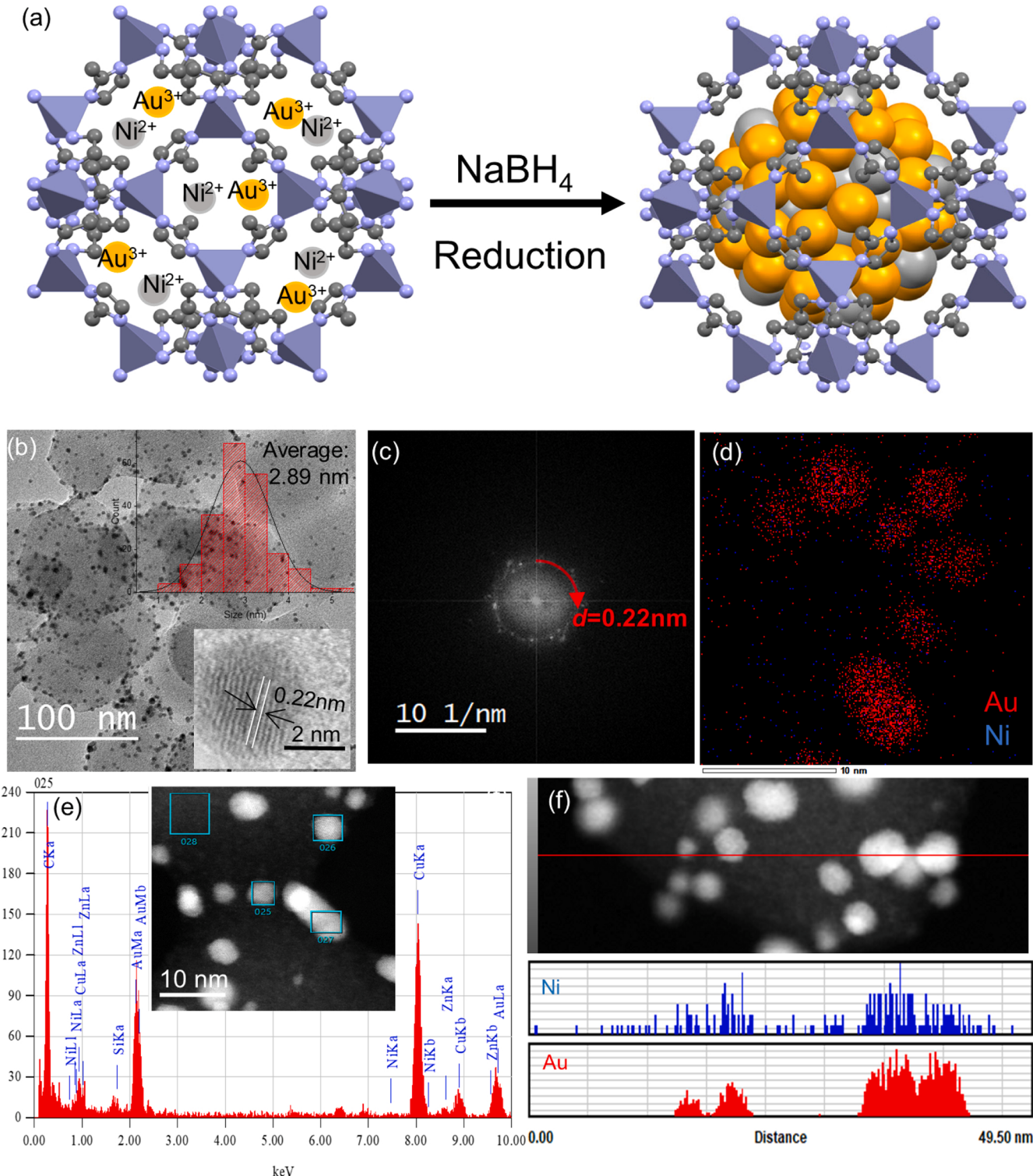


**Fig. 1.** (a) Synthesis of AuNi@ZIF-8; (b) TEM image of AuNi@ZIF-8 with size distribution and HAADF-STEM image inserted; (c) corresponding Fast Fourier Transform (FFT) pattern image of AuNi@ZIF-8; (d) Energy-Dispersive X-ray (EDX) mapping of different elements; (e) distributions of Au and Ni on 025 with the STEM image inserted. (f) HAADF-STEM image of AuNi@ZIF-8 and distributions of Au and Ni along cross-section lines.

latter two taking vibration frequencies from DFT. Finally, the reaction energies ( $G$ ) of different intermediates are defined as  $\Delta G = G_i - G_{\text{reactant}}$  ( $G_i$  is the energy of intermediates and  $G_{\text{reactant}}$  is the total energy of reactants).

### 3. Results and discussion

#### 3.1. Synthesis and characterization of the nanocatalysts

The synthesis of ZIF-8 was efficiently conducted according to previous reports upon mixing solutions of 2-methylimidazole and Zn ( $\text{NO}_3$ )<sub>2</sub> • 6 H<sub>2</sub>O [14], followed by rapid ZIF-8 precipitation (Fig. 1a); its framework structure was very stable in water and methanol [30]. The transmission electron microscopy (TEM) image in Fig. S2 shows that the ZIF-8 NPs are polyhedron nanocrystals and that their average size is 45.6 nm. The Au-based alloyed NPs supported on ZIF-8 were fabricated by the deposition-precipitation method producing a series of AuNi@ZIF-8 NPs with various Au and Ni percentages. The metal loading was determined by inductively coupled plasma-optical emission spectroscopy (ICP-AES, Table S1).

The TEM image in Fig. 1b shows that the AuNi NPs are packed in the ZIF-8 framework with an average size of 2.89 nm. The measured lattice distance of 0.22 nm corresponds to the (111) plane of AuNi NPs shown by the high-angle annular dark field scanning transmission electron microscopy (HAADF-STEM) image (insert in Fig. 1b). A distinct face center cubic (fcc) (111) phase for the AuNi NPs is confirmed by the fast Fourier transform pattern of AuNi@ZIF-8 (Fig. 1c). The corresponding STEM-EDX elemental mappings of AuNi@ZIF-8 display a distribution of Ni, Au elements throughout the AuNi NPs (Fig. 1d). Furthermore, the STEM-EDX mapping of a AuNi NP indicates that the Au and Ni elements are present in a single particle and that the distribution of Au and Ni

along cross-section lines of the AuNi NPs have an alloy structure in the ZIF-8 framework (Fig. 1e-f).

The X-ray powder diffraction (XRD, Fig. 2a) shows the typical crystal pattern of ZIF-8, and other ZIF-8-containing nanocatalysts have similar crystallinity as in Fig. 2a with ZIF-8 support. This suggests that the metal loading in the present case is low and that the NPs are inside ZIF-8. There are small changes in XRD spectra compared to pristine ZIF-8. The diffraction peak of Au@ZIF-8 at 38.1° corresponds to the Au (111) plane [36] with the addition of Ni to form the AuNi alloy; 20 increased to 39.1° in accordance with AuNi (111), which is in agreement with the HAADF-STEM result [37].

The specific Brunauer-Emmett-Teller (BET) surface areas of the various samples were determined by N<sub>2</sub> adsorption/desorption isothermal measurements. The pristine ZIF-8 framework exhibited apparent type-I N<sub>2</sub> isotherms with the N<sub>2</sub> uptake predominantly occurring at a rather low relative pressure range ( $P/P_0$  less than 0.03) (Fig. S3), indicating the presence of micropores within the structures. Fig. S3 presents the corresponding pore size distribution curves estimated by the non-local DFT model. The average size of the pore diameter is 1.6 nm, which is much smaller than the AuNi NP size (2.89 nm). The precursor metal cations are first introduced inside the ZIF cavity in which they interact with the N atoms of ZIF-8; then they are reduced by NaBH<sub>4</sub> [38] to NPs and, given their size, are trapped within the ZIF-8 cavity. Furthermore, after packing the AuNi NPs, the BET surface area decreases from 1787.3 m<sup>2</sup>·g<sup>-1</sup>–1011.3 m<sup>2</sup>·g<sup>-1</sup> (Fig. 2b and Table S2), due to the presence of AuNi NPs inside ZIF-8, which is consistent with previous reports [14,30]. All the results including those of TEM, significant BET surface decrease and pore width therefore indicate that the AuNi NPs are located inside the ZIF-8 framework.

X-ray Photoelectron Spectroscopy (XPS) shows binding energies of 83.2 eV and 86.8 eV for Au (0) 4 f<sub>7/2</sub> and Au (0) 4 f<sub>5/2</sub>, respectively, and

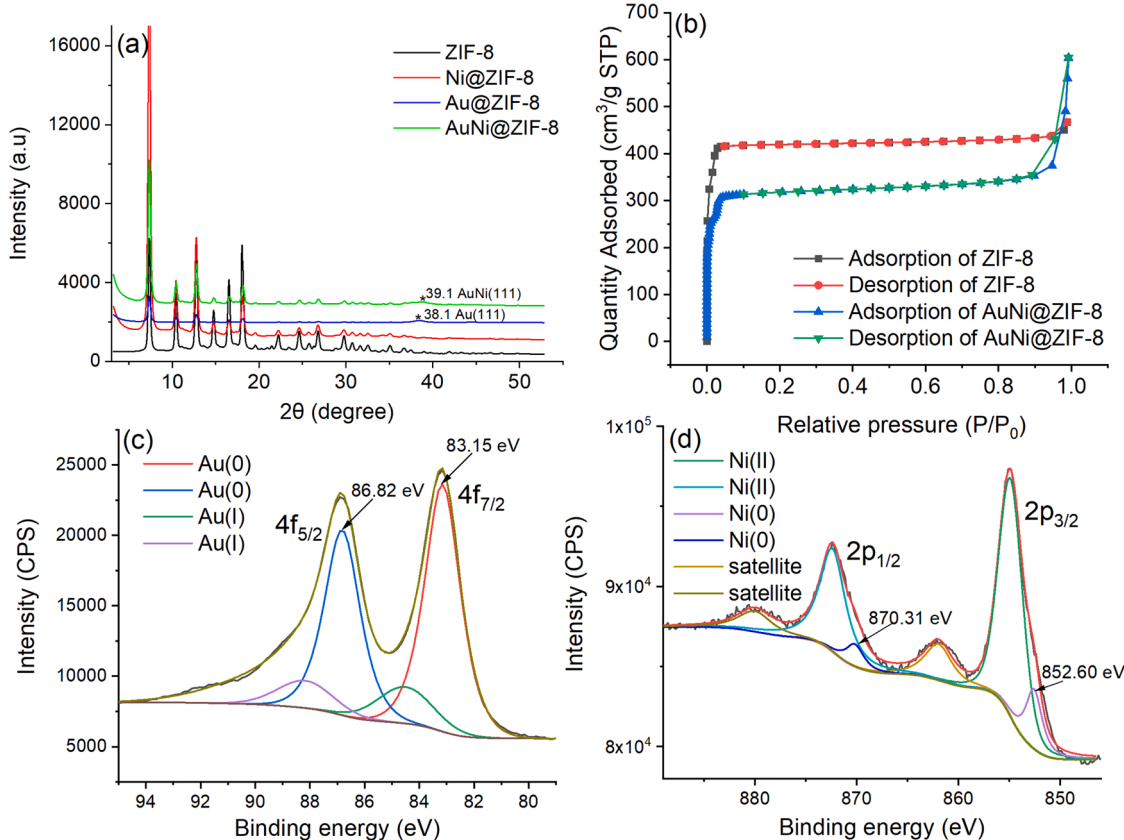


Fig. 2. (a) PXRD patterns of the prepared nanocatalysts. (b) Nitrogen adsorption-desorption isotherms of the nanocatalysts on ZIF-8 and AuNi@ZIF-8. (c) XPS spectra of AuNi@ZIF-8 in the Au 4 f region, (d) XPS spectra of AuNi@ZIF-8 in the Ni 2p region.

the binding energy of 852.6 and 870.3 eV confirms the presence of metallic Ni (0) in the AuNi@ZIF-8 NPs (Figs. 2c and 2d). The binding energy peaks of Au 4 f and Ni 2p also show the existence of the Au (I) and Ni (II) ions, attributed to some aerobic oxidation of the AuNi NPs, which has precedents [37,39,40]. The binding energies of Au 4 f (83.2 eV and 86.8 eV) of the AuNi alloy are shifted to lower values compared to those (84.0 eV and 87.3 eV) of AuNPs (Fig. S4), indicating strong electronic interaction between the Au and Ni atoms. The lower binding energies of Au 4 f for AuNi@ZIF-8 demonstrate that Au gains electron density upon alloying with Ni. The Ni 2p signals (852.6 eV and 870.3 eV) of the AuNi alloy are shifted to higher values compared to NiNPs (852.2 eV and 870.1 eV) [14] (Fig. S5), suggesting strong electronic interaction between the Ni and Au atoms and increased positively charged Ni center, which is in accord with a literature report [37]. XPS data after catalysis is discussed comparatively in Section 3.4.

### 3.2. Compared hydrolytic AB dehydrogenation catalyzed by a series of Au-based alloy NPs supported on ZIF-8

Searching for possible positive synergies in these alloyed nanocatalysts, we first chose to combine nanogold with non-noble late transition metals, these metals having priority as cheap, abundant and non-toxic elements. We compared Fe, Co, Ni and Cu which are modest

catalysts for AB hydrolysis. The nanocatalysts  $\text{Au}_{0.5}\text{Fe}_{0.5}$  @ZIF-8,  $\text{Au}_{0.5}\text{Co}_{0.5}$  @ZIF-8,  $\text{Au}_{0.5}\text{Ni}_{0.5}$  @ZIF-8 and  $\text{Au}_{0.5}\text{Cu}_{0.5}$  @ZIF-8 were probed immediately after their synthesis for AB hydrolysis. Only  $\text{Au}_{0.5}\text{Co}_{0.5}$  @ZIF-8 and  $\text{Au}_{0.5}\text{Ni}_{0.5}$  @ZIF-8 catalyzed quantitative  $\text{H}_2$  formation with a turnover frequency (TOF) value of  $40.0 \text{ mol}_{\text{H}_2} \cdot \text{mol}_{\text{cat}}^{-1} \cdot \text{min}^{-1}$  and  $2.4 \text{ mol}_{\text{H}_2} \cdot \text{mol}_{\text{cat}}^{-1} \cdot \text{min}^{-1}$ , respectively.  $\text{Au}_{0.5}\text{Fe}_{0.5}$  @ZIF-8 appears to be the least efficient among the four nanocatalysts. Indeed, after adding  $\text{Au}_{0.5}\text{Fe}_{0.5}$  @ZIF-8 into the AB hydrolysis medium, the NPs of  $\text{Au}_{0.5}\text{Fe}_{0.5}$  @ZIF-8 aggregated and rapidly precipitated due to their instability. Altogether, the order of catalytic activities found was:  $\text{Au}_{0.5}\text{Fe}_{0.5}$  @ZIF-8  $<$   $\text{Au}_{0.5}\text{Cu}_{0.5}$  @ZIF-8  $<$   $\text{Au}_{0.5}\text{Co}_{0.5}$  @ZIF-8  $<$   $\text{Au}_{0.5}\text{Ni}_{0.5}$  @ZIF-8 (Fig. 3). For the other catalysts including  $\text{Au}_{0.5}\text{Cu}_{0.5}$  @ZIF-8,  $\text{Au}_{0.5}\text{Co}_{0.5}$  @ZIF-8 and  $\text{Au}_{0.5}\text{Ni}_{0.5}$  @ZIF-8, the catalytic activity depended on the d-band center of the transition metal (Co, Ni and Cu). Indeed, among these three transition metals, Ni (001) showed the smallest d-band center ( $-1.18 \text{ eV}$ ) compared to Co (001) and Cu (001) [41]. After alloying with Au, the d-band center of AuNi is also smaller than those of AuCu and AuCo. The upgrading of the d-band center energy level of AuNi indicates that the antibonding energy state rises, leading to stronger binding between alloy surface and the adsorbate species, which means that the adsorption energy between AuNi and AB is stronger than those with AuCo and AuCu [42,43]. Therefore, this is consistent with the catalytic activity following

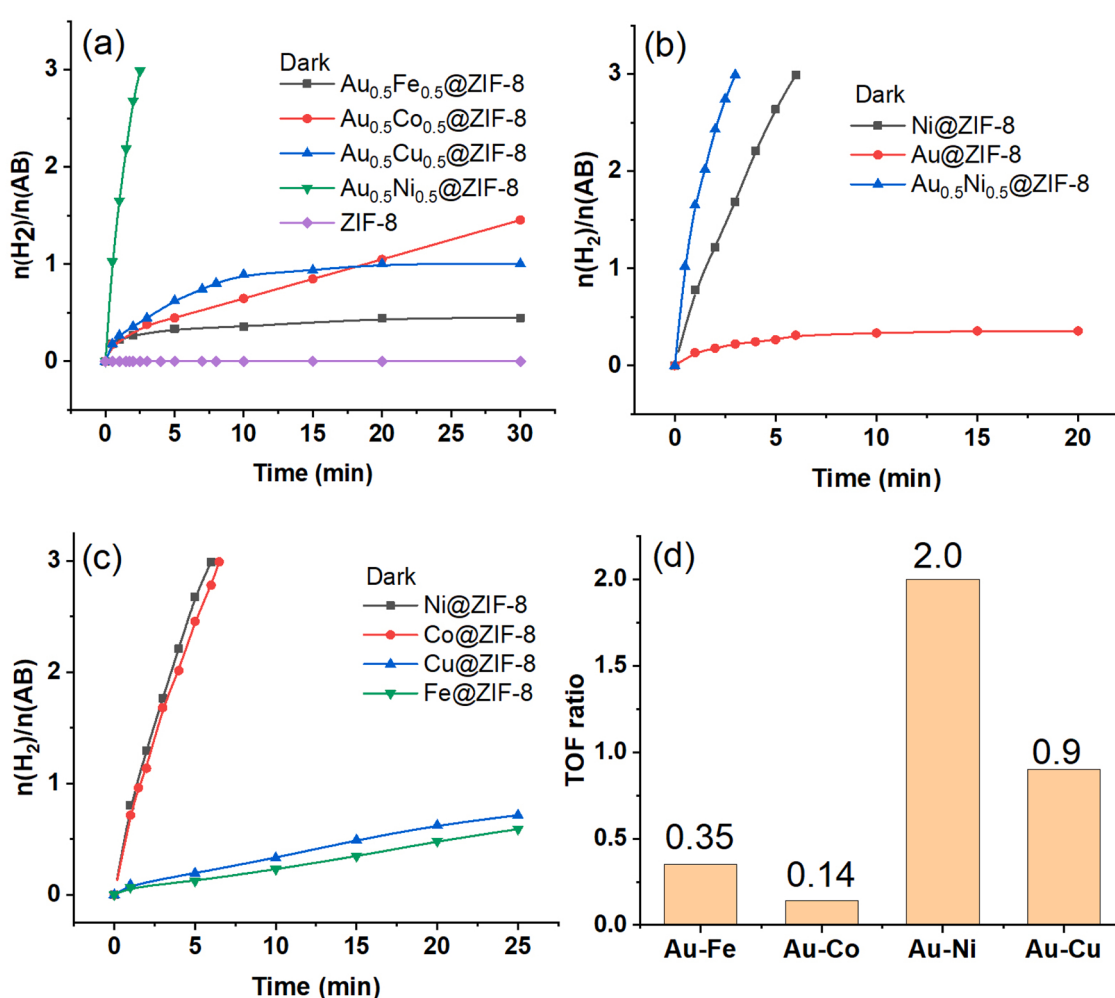


**Fig. 3.** (a) Plot of the molar amount of  $\text{H}_2$  generated upon AB hydrolysis vs. time catalyzed by ZIF-8 supported Au-based alloy NPs. (b) Comparison of the catalytic efficiencies among  $\text{Au}$  @ZIF-8,  $\text{Ni}$  @ZIF-8 and  $\text{Au}_{0.5}\text{Ni}_{0.5}$  @ZIF-8 without visible light irradiation. (c) Plot of the molar amount of  $\text{H}_2$  generated upon AB hydrolysis vs. time catalyzed by ZIF-8 supported monometallic NPs. (d) The synergistic effect is defined by the ratio TOF (alloy NPs)/TOF (monometallic NPs) with the support ZIF-8; when the TOF ratio is  $> 1$ , it means that there is a positive synergistic effect. Otherwise, there is no synergistic effect. In all the experiments, the reaction conditions are: 1 mmol of AB; 2.5% mmol MNP; temperature:  $25 \pm 0.5 \text{ }^\circ\text{C}$ .

the order:  $\text{Au}_{0.5}\text{Ni}_{0.5} @ \text{ZIF-8} > \text{Au}_{0.5}\text{Co}_{0.5} @ \text{ZIF-8} > \text{Au}_{0.5}\text{Cu}_{0.5} @ \text{ZIF-8}$ .

Alloying Au with either Co, Fe or Cu did not provide positive synergy in these alloys  $\text{Au}_{0.5}\text{Co}_{0.5} @ \text{ZIF-8}$ ,  $\text{Au}_{0.5}\text{Fe}_{0.5} @ \text{ZIF-8}$ ,  $\text{Au}_{0.5}\text{Cu}_{0.5} @ \text{ZIF-8}$ , respectively, that were less efficient than the corresponding monometallic catalyst  $\text{Co} @ \text{ZIF-8}$ ,  $\text{Fe} @ \text{ZIF-8}$  or  $\text{Cu} @ \text{ZIF-8}$  (Fig. 3). On the contrary, Fig. 3b shows that catalysis of AB hydrolysis proceeds much more efficiently with  $\text{Au}_{0.5}\text{Ni}_{0.5} @ \text{ZIF-8}$  than with the monometallic catalysts  $\text{Au} @ \text{ZIF-8}$  and  $\text{Ni} @ \text{ZIF-8}$ . The TOF value for  $\text{Au}_{0.5}\text{Ni}_{0.5} @ \text{ZIF-8}$  is  $40.0 \text{ mol}_{\text{H}_2} \cdot \text{mol}_{\text{cat}}^{-1} \cdot \text{min}^{-1}$ , which is twice more than that of  $\text{Ni} @ \text{ZIF-8}$  ( $20 \text{ mol}_{\text{H}_2} \cdot \text{mol}_{\text{cat}}^{-1} \cdot \text{min}^{-1}$ ), contrasting with the inefficiency of  $\text{Au} @ \text{ZIF-8}$  that showed almost no catalytic activity for this reaction (only 3.3% mol  $\text{H}_2$  evolution in 1 h), and the nil catalytic activity of pristine ZIF-8 (Figs. 3a and 3b). Here, the size of the NPs  $\text{Au} @ \text{ZIF-8}$ ,  $\text{Ni} @ \text{ZIF-8}$  and  $\text{Au}_{0.5}\text{Ni}_{0.5} @ \text{ZIF-8}$  were compared. The results showed that the  $\text{Au}_{0.5}\text{Ni}_{0.5} @ \text{ZIF-8}$  NPs are smaller than the  $\text{Ni} @ \text{ZIF-8}$  NPs and of size similar to the  $\text{Au} @ \text{ZIF-8}$  NPs, consistent with the higher catalytic activity of the  $\text{AuNi} @ \text{ZIF-8}$  NPs (Fig. S6 and S7). These results also show a strongly positive synergistic effect between Au and Ni alloyed in  $\text{Au}_{0.5}\text{Ni}_{0.5} @ \text{ZIF-8}$ , which originates from the strong electronic interaction between these two metals in ZIF-8, these electronic interactions being beneficial to the catalyst performances [19]. As a consequence, a quantitative amount of  $\text{H}_2$  evolved in 3 min with the catalyst  $\text{Au}_{0.5}\text{Ni}_{0.5} @ \text{ZIF-8}$  in the dark, whereas 6 min were needed with  $\text{Ni} @ \text{ZIF-8}$  under identical conditions.

### 3.3. Nanomaterial optimization for the catalysis of AB hydrolysis

In order to optimize the performance of the catalyst under dark conditions, the percentages of the two metals in the nanoalloys were varied. As shown in Fig. 4a, the efficiencies obtained upon AB hydrolysis were different with various AuNi compositions. Plotting the TOF as a function of the Au content reveals a sharp volcano-type curve appearing between the different alloy compositions, with a maximum for a composition involving equal molar amounts of Au and Ni (TOF<sub>i</sub>:  $40.0 \text{ mol}_{\text{H}_2} \cdot \text{mol}_{\text{cat}}^{-1} \cdot \text{min}^{-1}$  and TOF<sub>s</sub>:  $102.6 \text{ mol}_{\text{H}_2} \cdot \text{mol}_{\text{atom}}^{-1} \cdot \text{min}^{-1}$ ) (Fig. 4b and Table S3) [18].

The optimum of catalyst loading was investigated. Specifically, various loading amounts of  $\text{Au}_{0.5}\text{Ni}_{0.5} @ \text{ZIF-8}$  vs. ZIF-8 (3.7 wt%, 6.9 wt % and 13 wt%) were prepared, and the best performance was obtained with 6.9 wt% (Fig. S8). Furthermore, this Au-Ni nanocatalyst was supported by various other nanomaterials for comparison and optimization. Herein,  $\text{Au}_{0.5}\text{Ni}_{0.5} @ \text{graphene oxide (GO)}$ ,  $\text{Au}_{0.5}\text{Ni}_{0.5} @ \text{biochar}$  and  $\text{Au}_{0.5}\text{Ni}_{0.5} @ \text{SBA-15}$  were synthesized using the same method as that used with ZIF-8, the loading being also 6.9%. Fig. 4c shows that, among the four stabilizers, the best one is by far ZIF-8 finishing complete hydrolysis of AB with well-dispersed NPs. In contrast, with GO, biochar and SBA-15, the hydrolysis reaction could not be completed due to aggregation during the reactions. These comparisons suggest that ZIF-8 stabilizes and protects the AuNi NPs well from aggregation [41], contrary to the other above supports. Synergistic effects between Au and Ni were observed with all the supports, but the largest one was by far obtained with ZIF-8 as the support, and the TOF ratio between  $\text{Au}_{0.5}\text{Ni}_{0.5} @ \text{ZIF-8}$

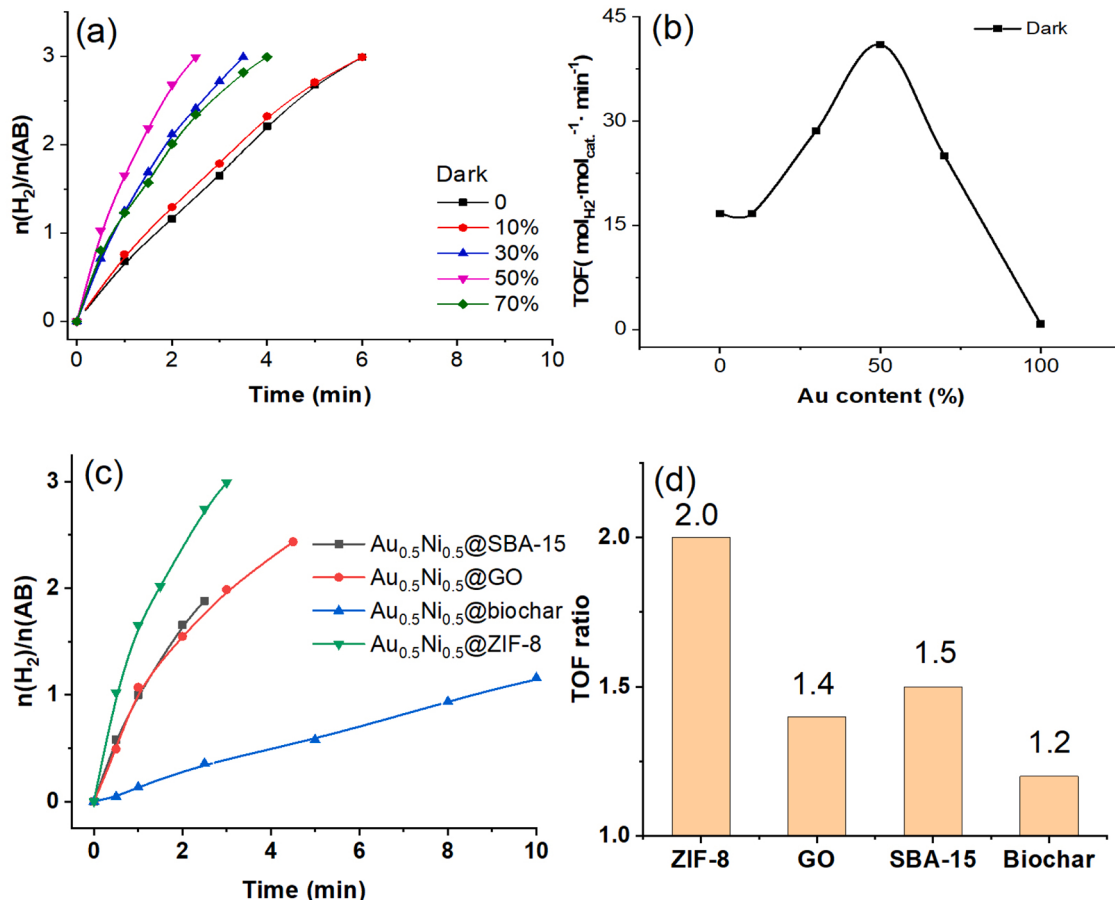


Fig. 4. (a) Plot of the molar amount of  $\text{H}_2$  generated upon AB hydrolysis vs. time catalyzed by  $\text{AuNi} @ \text{ZIF-8}$  with various ratios of Au and Ni without visible-light irradiation. (b) TOF values with different ratios of Au/Ni without visible-light irradiation. (c) AB hydrolysis catalyzed by AuNi on the various supports without visible light; (d) synergy effect defined by the ratio  $\{\text{TOF}(\text{AuNi})/\text{TOF}(\text{Ni})\}$ ; a ratio  $> 1$  means a positive synergy effect in the dark. In all the experiments, the reaction conditions were: 1 mmol of AB; 2.5% mmol MNP; temperature:  $25 \pm 0.5^\circ\text{C}$ .

@ ZIF-8 and Ni@ZIF-8 reached 2 (Fig. 4d). This indicates that ZIF-8 exhibits high selectivity with AuNi NPs for AB hydrolysis among all the supports, and this support exerted a strong synergistic cooperativity involving optimized stereo-electronic interactions, protection and accessibility in its cavity. Thus, altogether the optimized synergy is disclosed among the three nanocomponents Au, Ni and ZIF-8. This is rationalized as follows. ZIF-8 influences the interaction between Au and Ni by electronic ( $\sigma$ ) donation from the ZIF-8 imidazole N ligands inside the ZIF cavity that are coordinated to the NP surface [44]. This enrichment of the electronic density at the NP surface enhances the electronic-density-dependent surface Ni sites towards water activation [45], which is the rate-determining step of AB hydrolysis. Sterically, the role of ZIF-8 as NP support is to protect, by encapsulation, these particles from over aggregation, which is not the case for the other supports.

#### 3.4. Visible-light-induced acceleration of AuNi@ZIF-8-catalyzed AB hydrolysis

A low-power LED light was employed to irradiate the reaction medium in order to explore the plasmonic effect of the Au-based alloy catalytic NP system upon AB hydrolysis. Compared to the same reactions conducted without visible light irradiation, the efficiencies of all nanocatalyzed AB hydrolysis reactions were enhanced in the presence of visible light. The order of catalytic activity found was  $\text{Au}_{0.5}\text{Fe}_{0.5} @ \text{ZIF-8} < \text{Au}_{0.5}\text{Cu}_{0.5} @ \text{ZIF-8} < \text{Au}_{0.5}\text{Co}_{0.5} @ \text{ZIF-8} < \text{Au}_{0.5}\text{Ni}_{0.5} @ \text{ZIF-8}$

(Fig. 5a).

Impressively, the time for complete AB hydrolysis catalyzed by  $\text{Au}_{0.5}\text{Ni}_{0.5} @ \text{ZIF-8}$  was reduced from 3 min in the dark to 1 min 45 s with visible light irradiation (Fig. 5b). Table S4 shows that the catalytic activity of AuNi@ZIF-8 compares advantageously with those of previously recorded plasmonic metal-based photocatalysts for AB hydrolysis.

It is remarkable that, in comparison, visible light did not exert any beneficial role on AB hydrolysis catalyzed by monometallic Au@ZIF-8 or Ni@ZIF-8. This is indicated by the fact that the reaction rates of AB hydrolysis remain similar in the presence or absence of visible light for both monometallic catalysts in ZIF-8 (Fig. S9). In order to understand the light enhancement of the AB hydrolysis reaction rate selectively observed in the presence of the nanocatalyst  $\text{Au}_{0.5}\text{Ni}_{0.5} @ \text{ZIF-8}$  and not in the presence of monometallic ZIF-8 supported AuNPs or NiNPs, UV-vis. spectra of these three nanocatalysts were recorded (Fig. 5c). As a result, both Au@ZIF-8 and  $\text{Au}_{0.5}\text{Ni}_{0.5} @ \text{ZIF-8}$  show obvious plasmon bands, but the absorption curve of Ni@ZIF-8 is flat. Although the catalytic activity of Au@ZIF-8 is only small in the dark, there is no enhancement upon visible light illumination in the presence of this nanocatalyst. This means that whatever hot electrons are generated on the surface of Au atoms that transfer to other Au surface atoms, Au@ZIF-8 remains a rather inert catalyst for AB hydrolysis even upon plasmonic excitation by visible light. To explore the best ratio between the two metals for the AuNi@ZIF-8 alloys under visible-light irradiation, different compositions of AuNi NPs were used for catalysis of AB

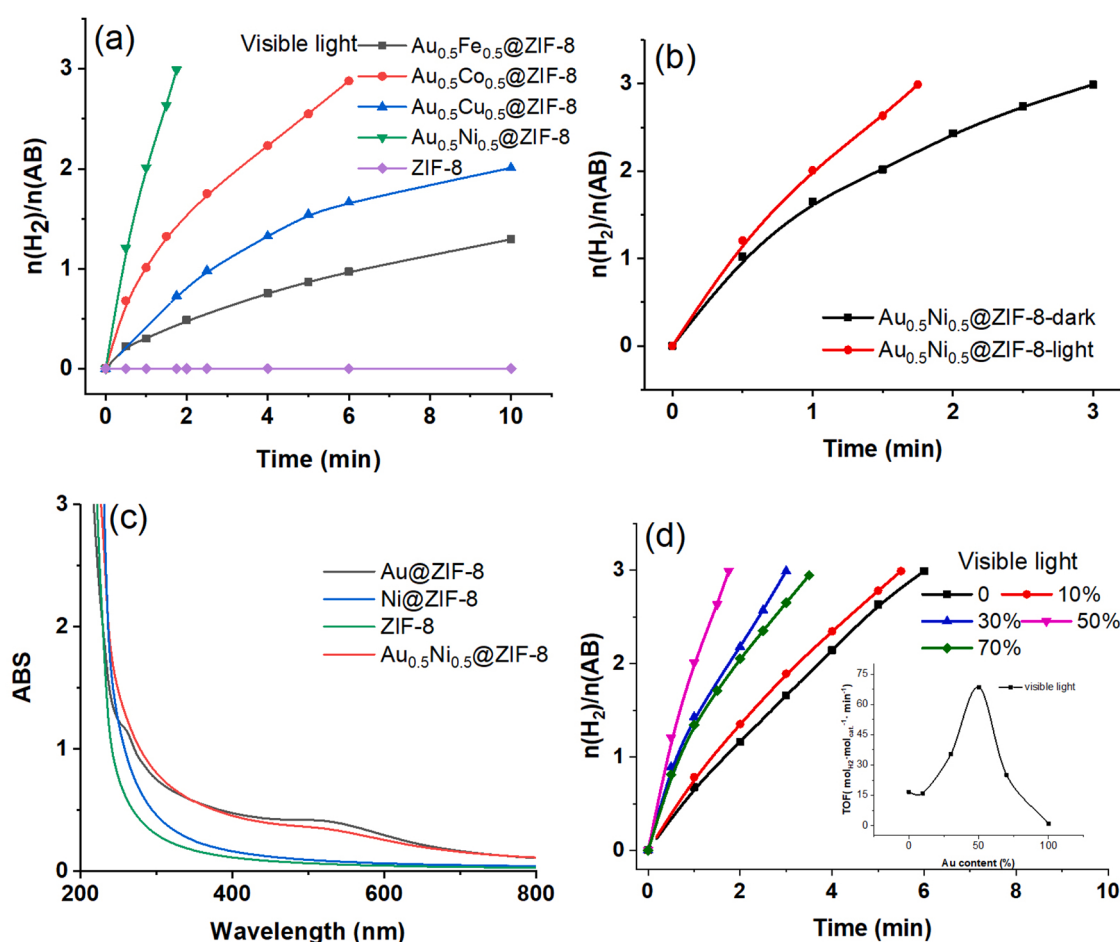


**Fig. 5.** (a) Plot of the molar amount of  $\text{H}_2$  generated upon AB hydrolysis vs. time catalyzed by ZIF-8 supported Au-based alloy NPs with visible light irradiation. (b) Comparison of the catalytic efficiencies of  $\text{Au}_{0.5}\text{Ni}_{0.5} @ \text{ZIF-8}$  under visible light irradiation and dark conditions. (c) UV-vis. spectra of Au@ZIF-8,  $\text{Au}_{0.5}\text{Ni}_{0.5} @ \text{ZIF-8}$ , and Ni@ZIF-8. (d) Plot of the molar amount of  $\text{H}_2$  generated upon AB hydrolysis vs. time catalyzed by  $\text{Au}_{0.5}\text{Ni}_{0.5} @ \text{ZIF-8}$  with various ratios of Au and Ni with visible-light irradiation and TOF values with different ratios of Au/Ni with visible-light irradiation. In all the experiments, the reaction conditions were: 1 mmol of AB; 2.5% mmol MNP; temperature:  $25 \pm 0.5^\circ\text{C}$ .

hydrolysis. As shown in Fig. 5d, the ratio of 1–1 underwent the best catalytic activity with a  $\text{TOF}_t$  of  $68.6 \text{ mol}_{\text{H}_2} \cdot \text{mol}_{\text{cat}}^{-1} \cdot \text{min}^{-1}$  and  $\text{TOF}_s$  of  $175.9 \text{ mol}_{\text{H}_2} \cdot \text{mol}_{\text{atom}}^{-1} \cdot \text{min}^{-1}$  (Fig. 5d and Table S3). Upon increasing the Au amount in the AuNi alloy, the whole catalytic activity of  $\text{Au}_{0.5}\text{Ni}_{0.5}$  @ZIF-8 decreased, because the AuNPs are a rather inert catalyst upon AB hydrolysis, although the introduction of Au enhances the plasmon of such catalysts. Therefore, the balance of plasmon and catalytic activity is concerned [26].

Under visible-light irradiation, rate enhancement was observed with the Au–Ni alloy only upon employing ZIF-8 as support, whereas light did not accelerate the reaction when GO and biochar were used for that purpose (Fig. S10). This is in accord with the fact that the AuNi alloy rapidly aggregates on other supports such as SBA-15, GO and biochar in the catalytic hydrolysis process. The UV–vis. spectra of all these supported nanocatalysts were recorded, and a plasmon band was observed for  $\text{Au}_{0.5}\text{Ni}_{0.5}$  @ZIF-8 ranging from 450 to 620 nm (Fig. S11). On the other hand, there were no plasmon band for  $\text{Au}_{0.5}\text{Ni}_{0.5}$  @GO or  $\text{Au}_{0.5}\text{Ni}_{0.5}$  @biochar. The UV–vis. spectra of the four supports were recorded in order to verify that the Localized Surface Plasmon Resonance (LSPR) comes from the AuNi alloy, i. e. not from the support alone. As shown in Fig. S12, all the support UV–vis. curves are flat, confirming that the LSPR is due to the AuNi alloy. However, both  $\text{Au}_{0.5}\text{Ni}_{0.5}$  @GO and  $\text{Au}_{0.5}\text{Ni}_{0.5}$  @biochar do not show plasmon bands in the UV–vis spectra. This is assigned to the very strong adsorption of GO and biochar (both black powders) in the UV–vis. region (Fig. S12), for which any plasmon band would be covered by GO and biochar. In contrast, the plasmon band was observed for  $\text{Au}_{0.5}\text{Ni}_{0.5}$  @ZIF-8, i. e. it was not obscured in the suspension (the ZIF-8 solid is white).

However, the support synergistically contributes to the overall LSPR as shown in Fig. 5c. One key feature of the plasmonic metal catalysts is that the performance depends on the wavelength of irradiation, since the light wavelength determines the energy of the incoming photons and thus the energy of the photogenerated charge carriers [42]. Thus, to verify the influence exerted by the plasmon-mediated catalyst, the catalytic efficiencies of AB hydrolysis were recorded under 450 nm, 520 nm and 620 nm light irradiation (Fig. S13). As a result, the 620 nm light is ineffective, which is shown by the fact that the reaction rate obtained using this light wavelength is the same as that of the reaction under dark conditions. By contrast, 450 nm and 520 nm light illuminations enhance the catalytic AB hydrolysis to some degree, which means that the visible light is only efficient within the range of the plasmon band of AuNi, further confirming the favorable role of the LSPR excitation in the photocatalytic system. The 520-nm light irradiation is more efficient than the 450-nm light in accelerating the hydrolytic

dehydrogenation of AB catalyzed by  $\text{Au}_{0.5}\text{Ni}_{0.5}$  @ZIF-8. Therefore, photon fluxes at different wavelengths were calculated here following a standard ferrioxalate actinometry for the analysis of the influence of the quantity of photons on photocatalysis [46]. This analysis revealed that the 450-nm irradiation ( $2.92 \times 10^{-9}$  einsteins.s<sup>-1</sup>) possesses a higher photon flux than the 520-nm one ( $2.34 \times 10^{-9}$  einsteins.s<sup>-1</sup>). This shows that irradiation with more photons does not contribute to increased efficiency, because it is only the light wavelength corresponding to the surface plasmon band of AuNi@ZIF-8 that provides enhanced catalytic efficiency. Indeed, the plasmon band of monometallic Au@ZIF-8 culminates at 530 nm, but upon alloying with Ni, it is broadened and culminates at 520 nm (Fig. 5c).

Usually, the plasmon-induced enhancement includes photo thermalization, photo local field and electron density transfer [47,48]. Thus, these three aspects need to be discussed here. The low-energy electrons couple to phonon modes after thermalization, increasing the temperature of the plasmonic metal, which is then dissipated to the environment. Therefore, in order to accurately demonstrate the influence of heating of the reactor itself upon continuous illumination, a temperature probe was placed inside the reaction flask to observe the temperature changes during AB hydrolysis over  $\text{Au}_{0.5}\text{Ni}_{0.5}$  @ZIF-8 (25 °C, 7 mW cm<sup>-1</sup>), and a temperature increase of less than 1 °C was observed over 5 min of irradiation (Fig. 6a). However, the efficient catalysts allowed delivery of hydrogen in reactions that were completed after only 1.75–3 min depending on the system. There was no significant increase in the hydrogen production rate at 26 °C compared to that recorded at 25 °C (Fig. 6b). Thus, it is concluded that the photothermal effect has no significant contribution to the visible light induced enhancement of the catalyzed AB dehydrogenation reaction.

The electric field, induced by the plasmon, is dominated by the local electronic states at the NP interface, and these surface plasmonic fields are beneficial to provide sufficient energy for the activation of some chemical bonds [28]. Moreover, the local electric field decays almost exponentially with the distance away from the NP surface, accompanied by the generation of a gradient force. The stronger field-gradient force is important to capture reactant molecules and polarize the trapping target [49]. Finite Difference Time Domain (FDTD) simulation was employed to calculate the SPR-related local electric fields. The  $|\mathbf{E}/\mathbf{E}_0|^2$  of AuNi is 8.7. The AuNiNP dimers exhibit a stronger near-field distribution compared with a single alloy particle, and  $|\mathbf{E}/\mathbf{E}_0|^2$  reaches up to 37.4 (Fig. S14). Thus, the enhanced field confers superior hot electron generation and adsorption of molecular substrates to the alloyed AuNi NPs. Specifically, the stronger molecular adsorption allows the formation of metal-adsorbent complexes (metal-AB water complexes) [22].

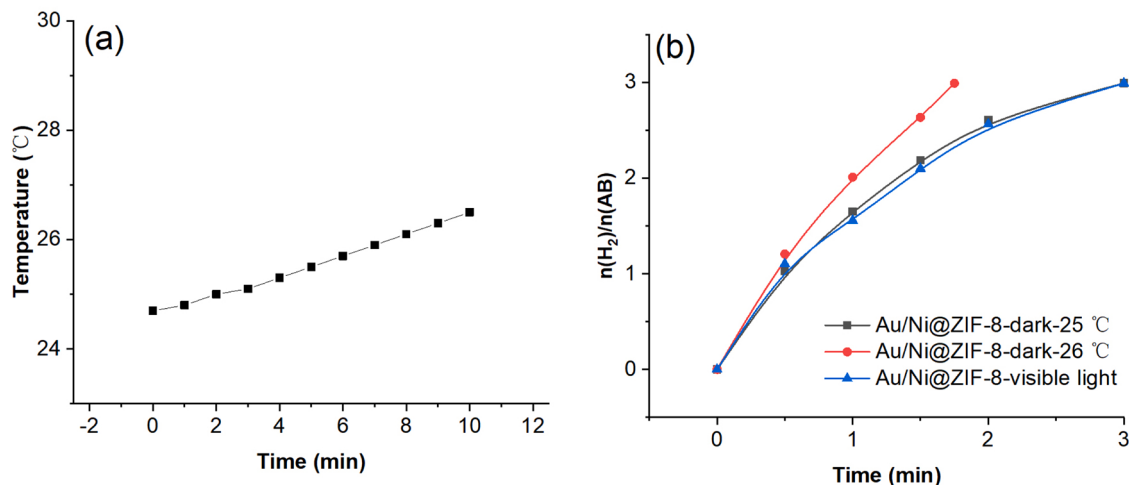


Fig. 6. (a) Temperature increase of the catalytic system under visible-light illumination. (b) Catalytic efficiency of AB hydrolysis by AuNi@ZIF-8 under different conditions. Reaction conditions: 1 mmol of AB; 1:1 of Au and Ni ratio; 2.5% mmol MNP.

Meanwhile, favorable adsorption of reactants onto metal NPs is important to enhance the catalytic activity. Zheng et al. found that the field enhancement is beneficial to the adsorption between substrates and metal atoms [47]. Similarly, in this case, significant field enhancement of alloyed AuNi NPs enhances the adsorption of the AB-H<sub>2</sub>O substrate, accelerating the energy transfer process and thus enhancing the catalytic activity.

The catalyst characterization by TEM and XPS were compared before and after light-accelerated reaction (Fig. 7 and S15). The TEM images show that the size of the AuNi NPs increased subsequent to light irradiation of the AB hydrolysis reaction medium from 2.89 nm before the reaction to 3.86 nm after reactions (Fig. S15). There was just a slight increase of NP size, as NPs tended to aggregate during the reaction, which has been reported in related publications, demonstrating the excellence of ZIF-8 as support [50,51]. Based on the result above, the durability of Au<sub>0.5</sub>Ni<sub>0.5</sub> @ZIF-8 was evaluated. As illustrated in Fig. S16, the catalyst Au<sub>0.5</sub>Ni<sub>0.5</sub> @ZIF-8 still showed high hydrogen production activity within 3 cycles. The XPS results show the presence of Au and Ni at the NP surface both before and after the reaction involving visible light irradiation. After the reaction, XPS shows binding energies of 87.2 and 83.5 eV for Au (0) 4 f<sub>7/2</sub> and Au (0) 4 f<sub>5/2</sub>, respectively, and the binding energies of 869.9 and 852.4 eV confirm that the valence state of Ni remains Ni (0) (Figs. 7c and 7d). Even if the valence state of Au and Ni did not change in the process of AB hydrolysis catalyzed by AuNi@ZIF-8, shifts of binding energy were observed as follows in the region of Au 4 f and Ni 2p. The binding energy of Au 4 f at 86.8 and 83.2 eV before reaction shifted after reaction to higher values (87.2 and 83.5 eV) (Figs. 7a and 7c), indicating that the Au atoms became more positively charged. Correlatively, the Ni 2p (870.3 and 852.6 eV) signals shifted to lower

values (869.9 and 852.4 eV) after reaction (Figs. 7b and 7d), demonstrating that there was an electronic simulation after the photoreaction. These shifts imply that electron density was transferred from Au to Ni during the light irradiation reaction process, and consequently Ni has been electronically enriched at the expense of Au, as indicated by comparison to monometallic Au and Ni NPs [46]. This shows that even if the time scale of the plasmon-induced electron transfer is only of the order of the fs, this electron density shift has some irreversible character after the photoreaction involved in the restructuration.

Concerning the heterogeneity of the catalyst in the reaction with visible-light irradiation, the electron transfer behavior that occurred between AuNiNPs and ZIF-8 was investigated. Comparison with the photocurrent density of pristine ZIF-8 and Au<sub>0.5</sub>Ni<sub>0.5</sub> @ZIF-8 during the several on-off cycles of visible light shows flat curves for both Au<sub>0.5</sub>Ni<sub>0.5</sub> @ZIF-8 and ZIF-8 (Fig. S17), and the photocurrent density is near to 0. This is taken into account by the fact that AuNi alloys are encapsulated by ZIF-8 that is an insulator. This indicates that ZIF-8 itself is not responsible for transferring and separating electrons induced by the LSPR of Au NPs, in accord with other reports [52,53]. ZIF-8 without any special treatment and addition is an insulator, i. e. it cannot be excited by visible light due to its high LUMO level, as reported [53]. Therefore, ZIF-8 cannot accept photo-generated electrons from Au NPs. The lack of observation of a photocurrent for Au<sub>0.5</sub>Ni<sub>0.5</sub> @ZIF-8 also confirmed this.

### 3.5. Kinetic study

The kinetic studies of the reactions were conducted with different dosages of catalyst, AB concentration and temperatures in the dark. The time plots of H<sub>2</sub> production are provided vs. various concentrations of

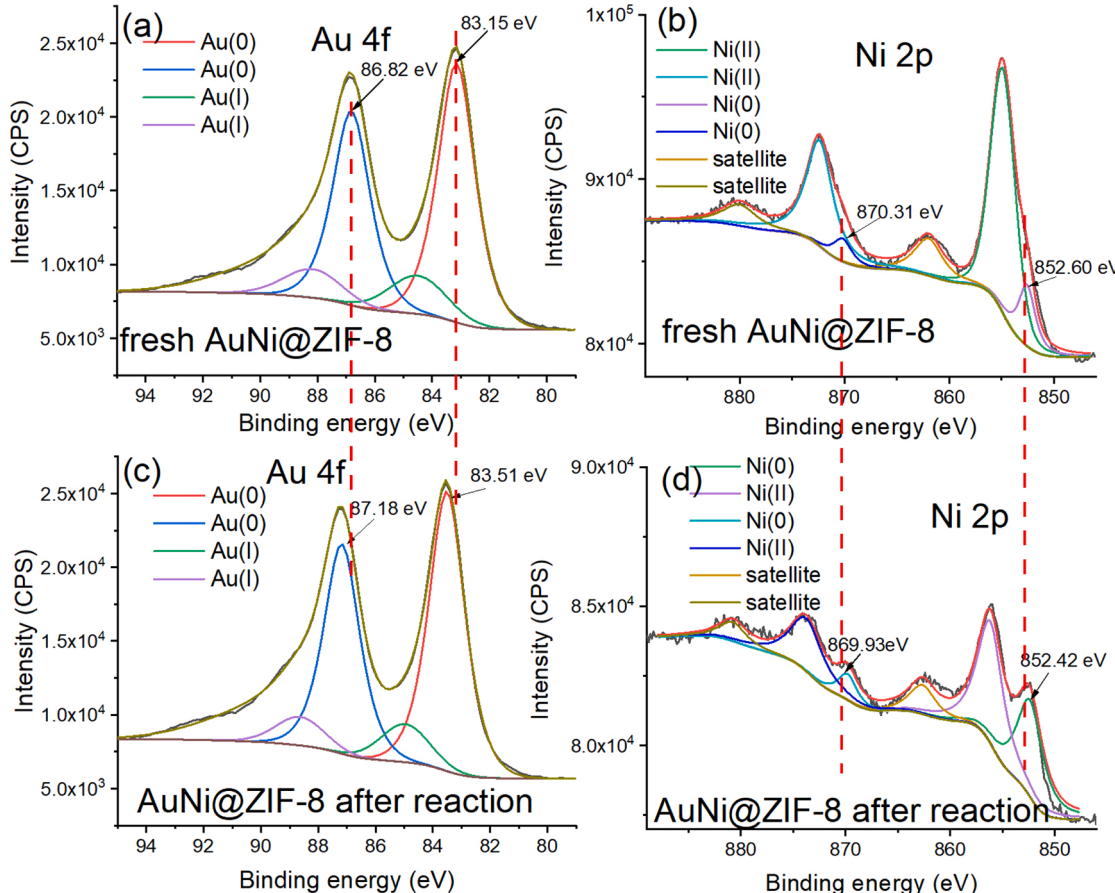


Fig. 7. XPS spectra of AuNi@ZIF-8, (a) Au 4 f region of AuNi@ZIF-8 before reaction, (b) Ni 2p region of AuNi@ZIF-8 before reaction, (c) Au 4 f region of AuNi@ZIF-8 after reaction, (d) Ni 2p region of AuNi@ZIF-8 after reaction.

AB with 2.5 mmol%  $\text{Au}_{0.5}\text{Ni}_{0.5}$  @ZIF-8 NPs. The reaction time is about 3 min for the different AB concentrations, and the logarithmic plot of  $\text{H}_2$  generation rate vs. concentration of AB is shown in Fig. S19a. The slope of the curve is 0.07, indicating that hydrolysis of AB catalyzed by  $\text{Au}_{0.5}\text{Ni}_{0.5}$  @ZIF-8 nearly follows zero-order kinetics in AB. The slope of the logarithmic plot of  $\text{H}_2$  generation vs. concentration of  $\text{Au}_{0.5}\text{Ni}_{0.5}$  @ZIF-8 NPs is 1.11 (Fig. S19b), leading to the result of a first-order reaction in catalyst concentration. The measurement of the time dependence of  $\text{H}_2$  generation at different temperatures is shown in Fig. S19c. According to the Arrhenius equation, the activation energy ( $E_a$ ) of AB hydrolysis is lower (approximately  $37.4 \pm 1.1 \text{ kJ/mol}$ ) with the catalyst  $\text{Au}_{0.5}\text{Ni}_{0.5}$  @ZIF-8 than with the monometallic  $\text{Ni}$ @ZIF-8 ( $42.7 \text{ kJ/mol}$ ) [14], showing that the positive synergy between Au, Ni and ZIF-8 is beneficial in reducing the activation energy.

### 3.6. Mechanistic study

Concerning the reaction mechanism of AB hydrolytic hydrogen release in the dark, several reports have indicated that one of the hydrogen atoms of  $\text{H}_2$  comes from AB and the other one from water [30, 54]. The kinetic isotope effect (KIE:  $k_{\text{H}}/k_{\text{D}}$ ) is an effective way to distinguish the rate-determining step (RDS) of a reaction [23, 55]. Herein,  $\text{D}_2\text{O}$  was used instead of  $\text{H}_2\text{O}$  involved in the AB hydrolysis catalyzed by  $\text{Au}_{0.5}\text{Ni}_{0.5}$  @ZIF-8. With  $\text{Au}_{0.5}\text{Ni}_{0.5}$  @ZIF-8 as the catalyst for AB hydrolysis in the dark, the KIE found with  $\text{D}_2\text{O}$  was 4 (Fig. 8), which is consistent with earlier studies. This primary KIE with high value leads to the suggestion of water O-H bond cleavage in the RDS [30]. Under visible-light irradiation, this KIE value raised to 4.3 (Fig. 8), which further confirms water bond breaking in the RDS, because the electron density on Ni atoms is enriched by the hot electron transmitted from the Au plasmon under visible-light illumination. Visible light boosts the reaction, and the KIE with  $\text{D}_2\text{O}$  should thus be enhanced compared to the KIE of the dark reaction, which was indeed found [26].

In order to track intermediate species, the Fourier-transformed infrared spectra (FT-IR) were recorded for the catalyst  $\text{Au}_{0.5}\text{Ni}_{0.5}$  @ZIF-8 to search for details of the hydrolysis process and the source of hydrogen. First, FT-IR was conducted, and the results are shown in Fig. S20. The B-H bonds assigned at 1080 and  $1177 \text{ cm}^{-1}$  disappeared upon prolonging the reaction time from 0 to 2 min. At the same time, the B-OH and B-O bonds that show peaks located at 1270 and  $1324 \text{ cm}^{-1}$  gradually appeared, demonstrating that the B-H bonds were cleaved and the B-O bonds were formed during the reaction [23]. Moreover, in order to confirm that one hydrogen atom of  $\text{H}_2$  is coming from water in the reaction of Eq. 1 and the other from AB, hydrogen evolution from AB catalyzed by  $\text{Au}_{0.5}\text{Ni}_{0.5}$  @ZIF-8 was conducted in a sealed two-chamber

reactor towards hydrogenation of styrene with the same catalyst whose optimization was indicated above (Fig. S21). In this hypothesis, HD gas would be generated upon AB hydrolysis catalyzed by  $\text{Au}_{0.5}\text{Ni}_{0.5}$  @ZIF-8 with  $\text{D}_2\text{O}$  as the solvent in the left tube and then would be transferred to the right tube in which hydrogenation of styrene proceeds in  $\text{CD}_3\text{OD}$ . The  $^1\text{H}$  NMR spectroscopy and gas chromatography-mass spectrometry analyses were used to detect the hydrogenation product in the right tube. The hydrogenation of styrene with generated hydrogen gas was successfully accomplished and was complete (quantitative) after 12 h at  $25^\circ\text{C}$  (Fig. S22-S23). Using the phenylethane methyl signals in the  $^1\text{H}$  NMR spectrum, the total number of H atoms found for the ethyl fragment is 4 because, from the 5 H atoms of this fragment, the fifth H atom being replaced by a D atom. Moreover, the major molecular peak of  $107 \text{ m/z}$  in the mass spectrum further indicates that one D atom was transferred to styrene producing mono-deuterated phenylethane (Fig. S24). These results fully confirm that one of the hydrogen atoms of  $\text{H}_2$  comes from AB and the other one from water. Furthermore, this present system shows that  $\text{Au}_{0.5}\text{Ni}_{0.5}$  @ZIF-8 is an efficient and versatile catalyst for this reaction.

The confirmation of the nature of the rate-determining step is a key challenge in the hydrogen generation process of AB. DFT calculation was conducted in order to confirm the corresponding mechanism (Fig. 9). The DFT calculation results show that the formation of  $^*\text{O}-\text{H}$  requires the highest reaction energy barrier both in dark and visible-light conditions for the three nanocatalysts  $\text{Au}$ @ZIF-8,  $\text{Ni}$ @ZIF-8 and  $\text{Au}_{0.5}\text{Ni}_{0.5}$  @ZIF-8 (Fig. 10). This result provides further evidence for the catalytic mechanism. Summarily, oxidative addition of the water O-H bond is the only rate-limiting step in AB hydrolysis for the targeted catalyst ( $\text{TS2} > \text{TS1}$ ). The optimized catalyst also provides an appropriate active site for the acceleration of the overall reaction via reducing the energy barrier of the RDS under light conditions. Upon visible light irradiation, a plasmonic hot electron is transferred from a gold atom to the excited state of the Ni-adsorbate ensemble, accelerating cleavage of the water  $\text{H}-\text{O}$  bond in the  $\text{NiH}-\text{H}-\text{OH}$  adsorbate by oxidative addition on Ni. Calculation of the Gibbs free energy under light condition, yields, compared to dark reaction,  $\text{TS1}_{\text{light}} < \text{TS1}_{\text{dark}}$ ,  $\text{TS2}_{\text{light}} < \text{TS2}_{\text{dark}}$ .

Upon catalysis, AB is expected to transfer a hydride ligand to either a Ni or Au site of the nanoalloy. This hydridic surface ligand is electrostatically bonded to an acidic H atom of water, which brings this water molecule close to the alloy surface towards more facile water O-H bond cleavage than in free water. It has been reported that OH NP surface ligand resulting from water cleavage prefers interacting with Ni(111) to form an ionic bond [56]. On the other hand, the alloy-H atom formed upon water cleavage is a covalent Ni-H bond due to the low oxophilicity of Ni sites on the alloy surface [57].

In the present work, the experiments above have shown the very low catalytic activity of  $\text{Au}$ @ZIF-8 compared to  $\text{Ni}$ @ZIF-8, therefore the Au atoms alone are not competitive for this O-H activation step, but the  $\text{AuNi}$ @ZIF-8 alloy is, forming hydrido and hydroxy surface ligands. Finally, the first hydrido surface ligand formed upon hydride transfer from AB and the second hydrido ligand formed upon water activation, eventually after “walking” near each other on the surface via successive bridging ( $\mu_2$ ) hydride bonds, reductively eliminate to form  $\text{H}_2$  [58]. (Scheme 1). From the XPS data, we know that the Au atoms are accepting charge transfer from Ni, which is only one parameter involved in water activation by the alloyed metals (vide infra). With visible-light irradiation, the generated hot electron resulting from the LSPR effect is transferred from Au to the Ni-adsorbate, enhancing electronic density on Ni, the water activation site. Furthermore, the electric field induced by the LSPR of  $\text{AuNi}$ @ZIF-8 generates energetic charge carriers, which is favorable for the adsorption of the reactants [28]. As a result, the cleavage of O-H bonds from  $\text{H}_2\text{O}$  (RDS) and B-H bonds from AB forming the intermediates M-H bonds and further reductive elimination are boosted by visible light irradiation to release  $\text{H}_2$ .

Contrary to  $\text{H}_2$  oxidative addition which is common and for instance working well here for styrene hydrogenation, H-OH oxidative addition

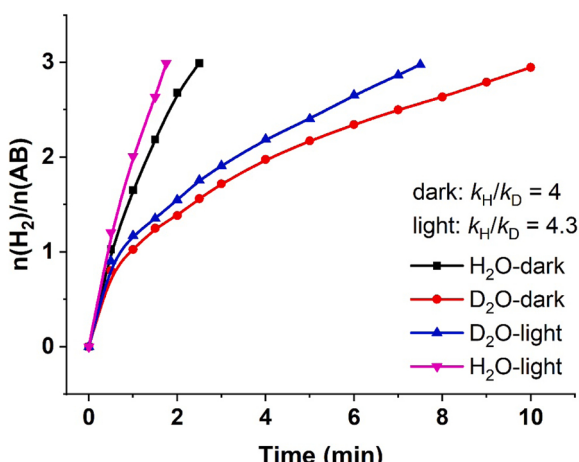
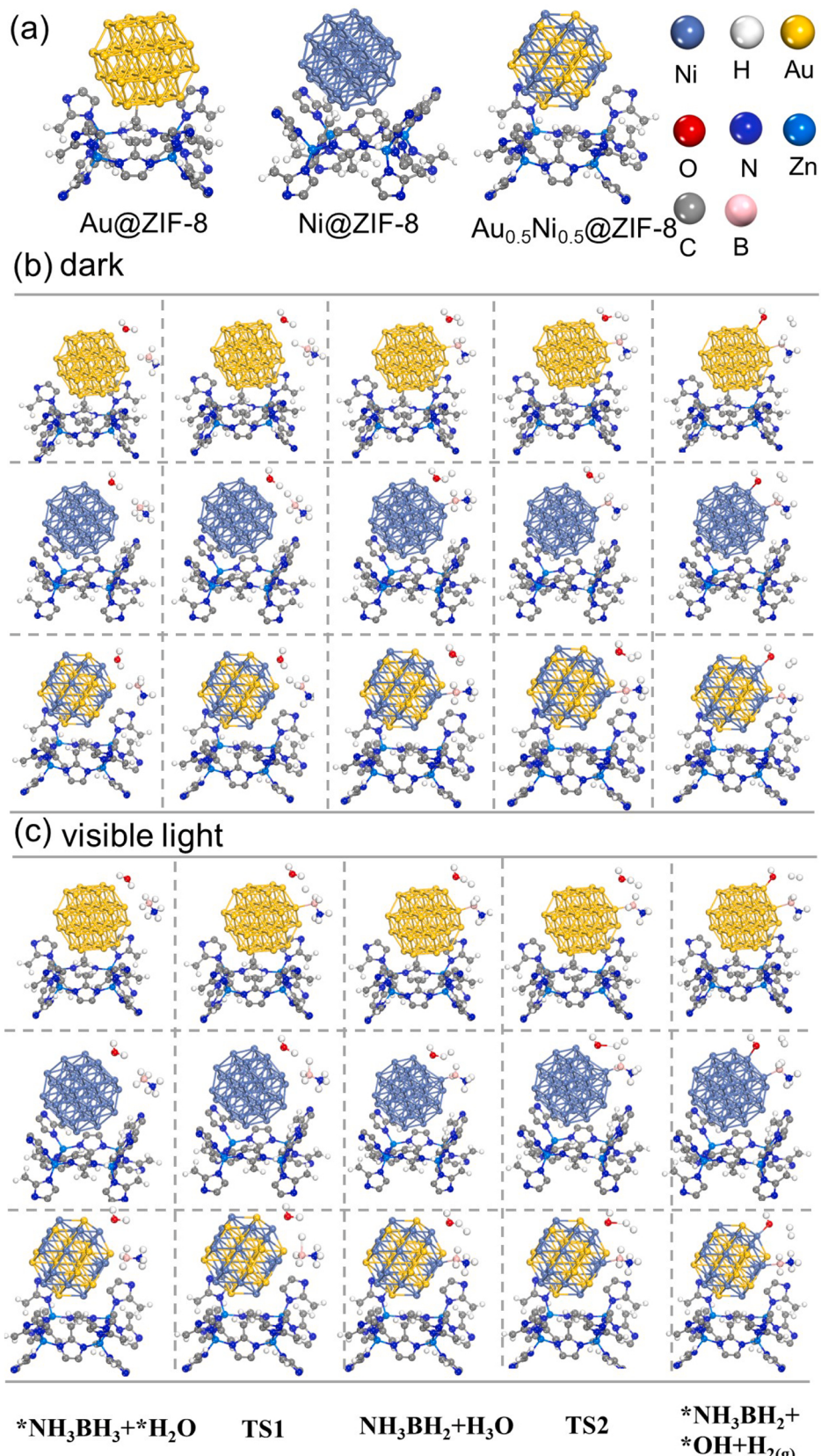
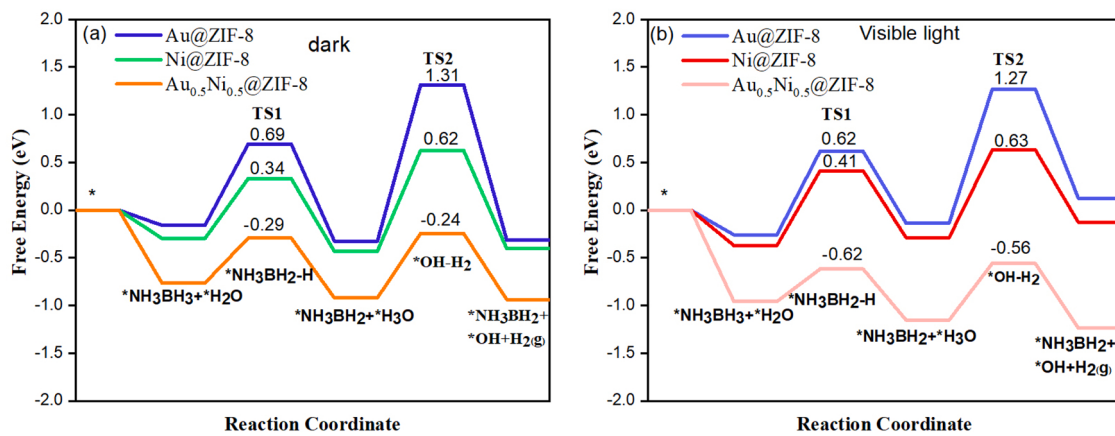


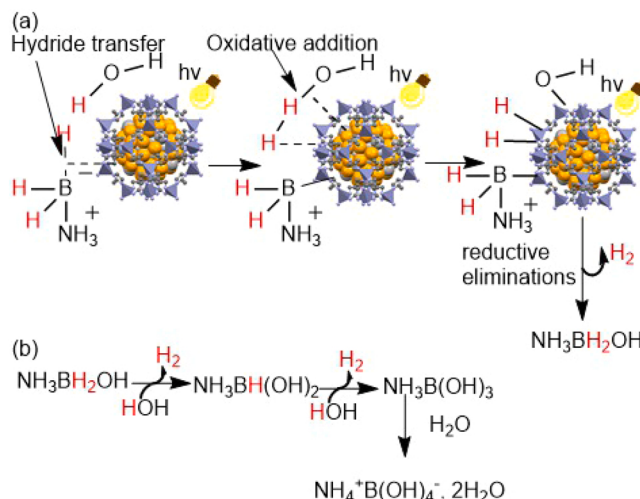
Fig. 8. Evolution of  $\text{H}_2$  upon AB hydrolysis with  $\text{H}_2\text{O}$  and  $\text{D}_2\text{O}$  catalyzed by  $\text{Au}_{0.5}\text{Ni}_{0.5}$  @ZIF-8 under visible light and dark.



**Fig. 9.** (a) Calculated (DFT) adsorption structures of Au@ZIF-8 (left), Ni@ZIF-8 (middle), and  $\text{Au}_{0.5}\text{Ni}_{0.5}@\text{ZIF-8}$  (right). (b) and (c) The 5 calculated intermediate structures for the reactions of  $\text{NH}_3\text{BH}_3$  and  $\text{H}_2\text{O}$  with the catalysts Au@ZIF-8 (top line), Ni@ZIF-8 (middle line), and  $\text{Au}_{0.5}\text{Ni}_{0.5}@\text{ZIF-8}$  (bottom line) (for their energy levels, see Fig 12) (b) under dark conditions; (c) with visible-light irradiation.



**Fig. 10.** DFT calculation for the free energy of  $\text{NH}_3\text{BH}_3$  and  $\text{H}_2\text{O}$  along their reaction catalyzed by  $\text{Au@ZIF-8}$ ,  $\text{Ni@ZIF-8}$ , and  $\text{Au}_{0.5}\text{Ni}_{0.5}@\text{ZIF-8}$  alloy, (a) under dark (left) and (b) with visible light excitation (right).



**Scheme 1.** Suggested mechanism for the visible-light-accelerated hydrolytic dehydrogenation of AB nanocatalyzed by  $\text{Au}_{0.5}\text{Ni}_{0.5}@\text{ZIF-8}$ .

(besides electroreduction) is a much more energetically demanding process, but it is known with a few mononuclear and binuclear noble-metal organo-bimetallic complexes (**Scheme 2**; case c) more or less mimics surface chemistry, although it is rarely encountered [59]. On the catalyst surface, the water, hydride and hydroxy ligands will likely be bonded in  $\mu_2$  or  $\mu_3$  fashion to surface atoms.

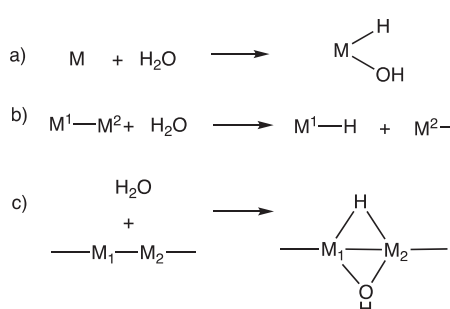
The adsorption energies  $E_H$  and  $E_{\text{OH}}$  play an important role in the activation process. For instance, the adsorption energy  $E_H$  is about  $-1.2$  eV on Ni and about  $0.2$ – $0.4$  eV on Au (slightly different depending

on the NP size) [60]. In this work, a strongly binding metal and a weakly binding metal are mixed in proportion (1/1) that were optimized for catalytic efficiency. Thus, a medium binding energy is obtained in the Au-Ni alloy (top of the volcano curve,  $-0.24$  eV in the dark;  $-0.54$  eV with visible light, from the present DFT study), and increased performances are indeed often obtained in nanocatalysis using such a strategy mixing a weakly binding and a strongly binding metal, for instance in AB hydrolysis catalyzed by Co-Pt [54] or Ni-Pt [30] alloys (i. e. mixing a late first-row transition metal and a noble metal) [61,62]. Likewise, reports on the simulations of electrochemical water dissociation showed that the activation energy correlated with the  $\text{OH}^*$  adsorption strength [63].

The possible reasons provoking the remarkably positive synergy between two metals in heterobimetallic alloys classically are the electronic effects, the strain effects and the ensemble effect. The electronic effects involve the transfer of electron density between the two metals, resulting in modification of the electronic structure and catalytic activity of the two atoms [64]. The strain effect involves a metallic surface layer, and it also modifies the electronic structure of the atoms by its effect on the width and the center of the d-band [65]. The ensemble effect has an impact on the catalytic activity, because it reflects atomic configurations on the NP surface, and it is essential and also impacts the electronic effects [66]. Concerning the important strain effect, the catalysis optimization shows that the d-band center position, which is related to the binding strength of the metal-adsorbate [67,68], here (AB—H-OH), is close to the Fermi level with the nanocatalyst  $\text{Au}_{0.5}\text{Ni}_{0.5}$  alloy in ZIF-8. The H-bonding between water and the metal hydride resulting from AB hydride transfer to the surface very much facilitates both the water adsorption and the weakening of the H-OH bond, both factors being very favorable for water activation. The ZIF-8 shell also introduces a drastic stereo-electronic factor for the substrate in the confined space between the ZIF-8 and the alloy surface that impacts the strain effect. The experienced sensitivity of the synergy to the nature of the support confirms this hypothesis.

#### 4. Conclusion

In conclusion, the unprecedented nanocatalysts,  $\text{AuNi}@\text{ZIF-8}$ , containing the plasmonic  $\text{AuNi}$  alloy and abundant metal Ni, have been optimized and shown here to efficiently catalyze fast AB hydrolysis producing  $\text{H}_2$  and other reactions. This nanocatalyzed  $\text{H}_2$  generation upon AB hydrolysis is boosted by the dramatic synergy between nanogold, nanonickel and ZIF-8 already in the dark, and the reaction is still very much accelerated by selective visible-light illumination using the  $\text{AuNi}$  plasmon. Yet, the light effect is selective, as only the light wavelengths corresponding to the plasmon band were shown to be active. Optimization of the support is shown with ZIF-8 that completely



**Scheme 2.** Schematic examples of water activation by noble-metal organo-metallic complexes (the ancillary ligands are omitted for clarity).

overtakes all the other supports in terms of beneficial synergy, due to both  $\sigma$  electronic donation from the ZIF-8 imidazole ligands and sterically by protective NP encapsulation. Excitation of the Au plasmon upon visible-light illumination induces hot electron transfer from Au to the Ni-AB-H-OH adsorbate assembly, still activating the reaction, particularly the rate-determining step, water O-H oxidative addition. Finally, the positive volcano-type synergy effect between the Ni, Au and ZIF-8 components and the plasmonic light rate acceleration effect best cumulate with the nanocatalyst  $\text{Au}_{0.5}\text{Ni}_{0.5}$  @ZIF-8. The previous successful use of Ni@ZIF-8 that allowed quantitative  $\text{H}_2$  generation in 6 min at 25 °C is boosted in this way to reach 1 min 45 s, which makes this ecofriendly method a very valuable one for convenient transport and quick  $\text{H}_2$  generation, and potentially also for many other organic reactions. The reaction mechanism was confirmed by the kinetic isotope effect and DFT calculations in the dark and in visible light to involve water oxidative addition on Ni as the rate-determining step. Such a spectacular activation by a Ni catalyst atom is all the more valuable for the replacement of palladium with this cheap metal as the price of palladium very recently almost doubled that of gold.

#### CRediT authorship contribution statement

**Naixing Kang:** Investigation, Verification, Formal analysis, Visualization, Writing – original Draft, Writing-review & editing, Formal analysis. **Xiaorong Wei:** Investigation. **Ruofan Shen:** Investigation, Formal analysis, Software. **Baojun Li:** Formal analysis, Software, Validation, Resources. **Eduardo Guisasola Cal:** Investigation, Formal analysis, Resources. **Sergio Moya:** Investigation, Formal analysis, Resources, Validation. **Lionel Salmon:** Investigation, Formal analysis, Validation. **Changlong Wang:** Investigation. **Emerson Coy:** Investigation, Visualization. **Murielle Berlande:** Investigation. **Jean-Luc Pozzo:** Supervision, writing – review & editing. **Didier Astruc:** Formal analysis, Resources, Supervision, Conceptualization, Project administration, writing – review & editing.

#### Declaration of Competing Interest

The authors declare that they have no known competing financial interests or personal relationships that could have appeared to influence the work reported in this paper.

#### Data Availability

No data was used for the research described in the article.

#### Acknowledgments

This article is dedicated to the memory of Professor François Mathey (1941–2020), a distinguished heterochemistry scientist. Helpful remarks and comments, particularly from one reviewer and from Dr Desire di Silvio, (CIC biomaGUNE, San Sebastian) and financial support from the China Scholarship Council (CSC, PhD grant to Naixin Kang), the National Science Centre of Poland under the program OPUS (2019/35/B/ST5/00248, Dr Emerson Coy and 2019/33/B/ST5/01495, Dr Sergio Moya), the MAT2017-88752-R Retos Project from the Ministerio de Economía, Industria y Competitividad, gobierno de España (Dr Sergio Moya), the National Natural Science Foundation of China (21401168, Prof. Baojun Li), the Centre National de la Recherche Scientifique (CNRS) and the University of Bordeaux are gratefully acknowledged.

#### Appendix A. Supporting information

Supplementary data associated with this article can be found in the online version at [doi:10.1016/j.apcatb.2022.121957](https://doi.org/10.1016/j.apcatb.2022.121957).

#### References

- [1] T. He, P. Pachfule, H. Wu, Q. Xu, P. Chen, Hydrogen carriers, *Nat. Rev. Mater.* 1 (2016) 1–17.
- [2] Q.-L. Zhu, Q. Xu, Liquid organic and inorganic chemical hydrides for high-capacity hydrogen storage, *Energy Environ. Sci.* 8 (2015) 478–512.
- [3] Q. Wang, D. Astruc, State of the art and prospects in metal-organic framework (MOF)-based and MOF-derived nanocatalysis, *Chem. Rev.* 120 (2020) 1438–1511.
- [4] W. Xu, W. Li, H. Wen, J. Ding, Y. Liu, W. Li, B. Li, Metal/metal-organic framework interfacial ensemble-induced dual site catalysis towards hydrogen generation, *Appl. Catal. B-Environ.* 286 (2021), 119946.
- [5] W.-W. Zhan, Q.-L. Zhu, Q. Xu, Dehydrogenation of ammonia borane by metal nanoparticle catalysts, *ACS Catal.* 6 (2016) 6892–6905.
- [6] Q. Yao, Z.-H. Lu, W. Huang, X. Chen, J. Zhu, High Pt-like activity of the Ni/Mo/graphene catalyst for hydrogen evolution from hydrolysis of ammonia borane, *J. Mater. Chem. A* 4 (2016) 8579–8583.
- [7] Z. Huang, S. Wang, R.D. Dewhurst, N.V. Ignat'ev, M. Finze, H. Braunschweig, Boron: Its Role in Energy-Related Processes and Applications, in: *Angew. Chem. Int. Ed.* 59, 2020, pp. 8800–8816.
- [8] A. Staubitz, A.P.M. Robertson, I. Manners, Ammonia-borane and related compounds as dihydrogen sources, *Chem. Rev.* 110 (2010) 4079–4124.
- [9] C. Wang, D. Astruc, Recent developments of nanocatalyzed liquid-phase hydrogen generation, *Chem. Soc. Rev.* 50 (2021) 3437–3484.
- [10] C.W. Hamilton, R.T. Baker, A. Staubitz, I. Manners, B-N compounds for chemical hydrogen storage, *Chem. Soc. Rev.* 38 (2009) 279–293.
- [11] F. Yao, S. Guan, L. Bian, Y. Fan, X. Liu, H. Zhang, B. Li, B. Liu, Ensemble-exciting effect in Pd/alk-Ti3C2 on the activity for efficient hydrogen production, *ACS Sustain. Chem. Eng.* 9 (2021) 12332–12340.
- [12] Q. Sun, N. Wang, Q. Xu, J. Yu, Nanopore-supported metal nanocatalysts for efficient hydrogen generation from liquid-phase chemical hydrogen storage materials, *Adv. Mater.* 32 (2020), 2001818.
- [13] C.Y. Alpaydin, S.K. Gulbay, C.O. Colpan, A review on the catalysts used for hydrogen production from ammonia borane, *Int. J. Hydrol. Energy* 45 (2020) 3414–3434.
- [14] C. Wang, J. Tuninetti, Z. Wang, C. Zhang, R. Ciganda, L. Salmon, S. Moya, J. Ruiz, D. Astruc, Hydrolysis of ammonia-borane over Ni/ZIF-8 nanocatalyst: high efficiency, mechanism, and controlled hydrogen release, *J. Am. Chem. Soc.* 139 (2017) 11610–11615.
- [15] M. Li, S.B. Zhang, J.K. Zhao, H. Wang, Maximizing metal-support interactions in Pt/Co3O4 nanocages to simultaneously boost hydrogen production activity and durability, *ACS Appl. Mater. Interfaces* 13 (2021) 57362–57371.
- [16] C. Wang, Y. Ren, J. Zhao, S. Sun, X. Du, M. Wang, G. Ma, H. Yu, L. Li, X. Yu, Oxygen vacancy-attired dual-active-sites Cu/Cu<sub>0.76</sub>Co<sub>0.24</sub>O<sub>4</sub> drives electron transfer for efficient ammonia borane dehydrogenation, *Appl. Catal. B Environ.* (2022), 121494.
- [17] S. Zhang, M. Li, J. Zhao, H. Wang, X. Zhu, J. Han, X. Liu, Plasmonic AuPd-based Mott-Schottky photocatalyst for synergistically enhanced hydrogen evolution from formic acid and aldehyde, *Appl. Catal. B Environ.* 252 (2019) 24–32.
- [18] Y. Kang, B. Jiang, J. Yang, Z. Wan, J. Na, Q. Li, H. Li, J. Henzie, Y. Sakka, Y. Yamauchi, T. Asahi, Amorphous alloy architectures in pore walls: mesoporous amorphous NiCo<sub>3</sub> alloy spheres with controlled compositions via a chemical reduction, *ACS Nano* 14 (2020) 17224–17232.
- [19] X. Huang, Y. Liu, H. Wen, R. Shen, S. Mehdi, X. Wu, E. Liang, X. Guo, B. Li, Ensemble-boosting effect of Ru-Cu alloy on catalytic activity towards hydrogen evolution in ammonia borane hydrolysis, *Appl. Catal. B-Environ.* 287 (2021), 11960.
- [20] Y. Yuan, L. Sun, G. Wu, Y. Yuan, W. Zhan, X. Wang, X. Han, Engineering nickel/palladium heterojunctions for dehydrogenation of ammonia borane: improving the catalytic performance with 3D mesoporous structures and external nitrogen-doped carbon layers, *Inorg. Chem.* 59 (2020) 2104–2110.
- [21] C. Cui, Y. Liu, S. Mehdi, H. Wen, B. Zhou, J. Li, B. Li, Enhancing effect of Fe-doping on the activity of nano Ni catalyst towards hydrogen evolution from NH<sub>3</sub>BH<sub>3</sub>, *Appl. Catal. B-Environ.* 265 (2020), 118612.
- [22] K. Guo, Y. Ding, J. Luo, M. Gu, Z. Yu, NiCu bimetallic nanoparticles on silica support for catalytic hydrolysis of ammonia borane: composition-dependent activity and support size effect, *ACS Appl. Energy Mater.* 2 (2019) 5851–5861.
- [23] S. Zhang, M. Li, L. Li, F. Dushimimana, J. Zhao, S. Wang, J. Han, X. Zhu, X. Liu, Q. Ge, H. Wang, Visible-light-driven multichannel regulation of local electron density to accelerate activation of O-H and B-H bonds for ammonia borane hydrolysis, *ACS Catal.* 10 (2020) 14903–14915.
- [24] S. Rej, C. Hsia, T. Chen, F. Lin, J. Huang, M.H. Huang, Facet-dependent and light-assisted efficient hydrogen evolution from ammonia borane using gold-palladium core-shell nanocatalysts, *Angew. Int. Ed. Chmie* 30013 (2016) 7222–7226.
- [25] P. Verma, K. Yuan, Y. Kuwahara, K. Mori, H. Yamashita, Enhancement of plasmonic activity by Pt/Ag bimetallic nanocatalyst supported on mesoporous silica in the hydrogen production from hydrogen storage material, *Appl. Catal. B-Environ.* 223 (2018) 10–15.
- [26] N. Kang, Q. Wang, R. Djeda, W. Wang, F. Fu, M.M. Moro, M. de los A. Ramirez, S. Moya, E. Coy, L. Salmon, J.-L. Pozzo, D. Astruc, Visible-light acceleration of H-2 evolution from aqueous solutions of inorganic hydrides catalyzed by gold-transition-metal nanoalloys, *ACS Appl. Mater. Interfaces* 12 (2020) 53816–53826.
- [27] C. Wang, D. Astruc, Nanogold plasmonic photocatalysis for organic synthesis and clean energy conversion, *Chem. Soc. Rev.* 43 (2014) 7188–7216.
- [28] L. Mascaretti, A. Dutta, S. Kment, V.M. Shalaev, A. Boltasseva, R. Zboril, A. Naldoni, Plasmon-enhanced photoelectrochemical water splitting for efficient renewable energy storage, *Adv. Mater.* 31 (2019), 1805513.

[29] M.C. Daniel, D. Astruc, Gold nanoparticles: assembly, supramolecular chemistry, quantum-size-related properties, and applications toward biology, catalysis, and nanotechnology, *Chem. Rev.* 104 (2004) 293–346.

[30] F. Fu, C. Wang, Q. Wang, A.M. Martinez-Villacorta, A. Escobar, H. Chong, X. Wang, S. Moya, L. Salmon, E. Fouquet, J. Ruiz, D. Astruc, Highly selective and sharp volcano-type synergistic Ni2Pt@ZIF-8-catalyzed hydrogen evolution from ammonia borane hydrolysis, *J. Am. Chem. Soc.* 140 (2018) 10034–10042.

[31] C. Wang, R. Ciganda, L. Yate, J. Tuninetti, V. Shalabaeva, L. Salmon, S. Moya, J. Ruiz, D. Astruc, Redox synthesis and high catalytic efficiency of transition-metal nanoparticle-graphene oxide nanocomposites, *J. Mater. Chem. A* 5 (2017) 21947–21954.

[32] R.P. Lopes, T. Guimarães, D. Astruc, Magnetized biochar as a gold nanocatalyst support for p-nitrophenol reduction, *J. Braz. Chem. Soc.* 32 (2021) 1680–1686.

[33] B. Delley, From molecules to solids with the DMol 3 approach, *J. Chem. Phys.* 113 (2000) 7756–7764.

[34] J.P. Perdew, K. Burke, M. Ernzerhof, Generalized gradient approximation made simple, *Phys. Rev. Lett.* 77 (1996) 3865–3868.

[35] S. Grimme, Semiempirical GGA-type density functional constructed with a long-range dispersion correction, *J. Comput. Chem.* 27 (2006) 1787–1799.

[36] Q. Zhang, Y. Zhang, K. Xiao, Z. Meng, W. Tong, H. Huang, Q. An, Plasmonic gold particle generation in layer-by-layer 2D titania films as an effective immobilization strategy of composite photocatalysts for hydrogen generation, *Chem. Eng. J.* 358 (2019) 389–397.

[37] J. Hao, H. Zhu, Y. Li, P. Liu, S. Lu, F. Duan, W. Dong, Y. Lu, T. Liu, M. Du, Tuning the electronic structure of AuNi homogeneous solid-solution alloy with positively charged Ni center for highly selective electrochemical CO<sub>2</sub> reduction, *Chem. Eng. J.* 404 (2021) 126523.

[38] P. Michaud, D. Astruc, J.H. Ammeter, Electron-transfer pathways in the reduction of d<sub>6</sub> and d<sub>7</sub> organoiron cations by LiAlH<sub>4</sub> and NaBH<sub>4</sub>, *J. Am. Chem. Soc.* 104 (1982) 3755–3757.

[39] J.L. Wang, F.Y. Chen, Y.C. Jin, R.L. Johnston, Highly active and stable AuNi dendrites as an electrocatalyst for the oxygen reduction reaction in alkaline media, *J. Mater. Chem. A* 4 (2016) 17828–17837.

[40] G. Darabdhara, M.R. Das, M.A. Amin, G.A.M. Mersal, N.Y. Mostafa, S.S. Abd El-Rehim, S. Szunerits, R. Boukherroub, Au-Ni alloy nanoparticles supported on reduced graphene oxide as highly efficient electrocatalysts for hydrogen evolution and oxygen reduction reactions, *Int. J. Hydrom. Energy* 43 (2018) 1424–1438.

[41] C. Wang, X. Liu, Y. Wu, D. Astruc, PtNi@ZIF-8 nanocatalyzed high efficiency and complete hydrogen generation from hydrazine borane: origin and mechanistic insight (Adv. article), *J. Mater. Chem. A* (2022), <https://doi.org/10.1039/D2TA04411K>.

[42] X. Zhang, Y. Zhao, X. Jia, Y. Zhao, L. Shang, Q. Wang, G.I.N. Waterhouse, L. Wu, C. Tung, T. Zhang, Silica-protected ultrathin Ni<sub>3</sub>FeN nanocatalyst for the efficient hydrolytic dehydrogenation of NH<sub>3</sub>BH<sub>3</sub>, *Adv. Energy Mater.* 8 (2018), 1702780.

[43] Z. Chen, Y. Song, J. Cai, X. Zheng, D. Han, Y. Wu, Y. Zang, S. Niu, Y. Liu, J. Zhu, Tailoring the d-band centers enables Co<sub>4</sub>N nanosheets to be highly active for hydrogen evolution catalysis, *Angew. Chem.* 130 (2018) 5170–5174.

[44] K.S. Park, Z. Ni, A.P. Côté, J.Y. Choi, R. Huang, F.J. Uribe-Romo, H.K. Chae, M. O’Keefe, O.M. Yaghi, Exceptional chemical and thermal stability of zeolitic imidazolate frameworks, *Proc. Natl. Acad. Sci.* 103 (2006) 10186–10191.

[45] F.I. Pambudi, Electronic properties of heterometallic zeolitic imidazolate framework and its encapsulation with Ni, Pd and Pt, *Inorg. Chem. Commun.* 143 (2022), 109798.

[46] T. Cornilleau, P. Hermange, E. Fouquet, Gold-catalysed cross-coupling between aryl diazonium salts and arylboronic acids: Probing the usefulness of photoredox conditions, *Chem. Commun.* 52 (2016) 10040–10043.

[47] F. Tong, X. Liang, Z. Wang, Y. Liu, P. Wang, H. Cheng, Y. Dai, Z. Zheng, B. Huang, Probing the mechanism of plasmon-enhanced ammonia borane methanolysis on a CuAg alloy at a single-particle level, *ACS Catal.* 11 (2021) 10814–10823.

[48] P. Xu, W. Lu, J. Zhang, L. Zhang, Efficient hydrolysis of ammonia borane for hydrogen evolution catalyzed by plasmonic Ag@Pd core-shell nanocubes, *ACS Sustain. Chem. Eng.* 8 (2020) 12366–12377.

[49] F.X. Tong, X.Z. Liang, M. Liu, Z.Y. Wang, Y.Y. Liu, P. Wang, H.F. Cheng, Y. Dai, Z. K. Zheng, B.B. Huang, Plasmon-enhanced water activation for hydrogen evolution from ammonia-borane studied at a single-particle level, *ACS Catal.* 12 (2022) 3558–3565.

[50] L. Zhou, N. Li, G. Owens, Z. Chen, Simultaneous removal of mixed contaminants, copper and norfloxacin, from aqueous solution by ZIF-8, *Chem. Eng. J.* 362 (2019) 628–637.

[51] H. Dai, X. Yuan, L. Jiang, H. Wang, J. Zhang, T. Xiong, Recent advances on ZIF-8 composites for adsorption and photocatalytic wastewater pollutant removal: fabrication, applications and perspective, *Coord. Chem. Rev.* 441 (2021), 213985.

[52] Y. Zhang, Q. Li, C. Liu, X. Shan, X. Chen, W. Dai, X. Fu, The promoted effect of a metal-organic frameworks (ZIF-8) on Au/TiO<sub>2</sub> for CO oxidation at room temperature both in dark and under visible light irradiation, *Appl. Catal. B Environ.* 224 (2018) 283–294.

[53] M. Wen, S. Song, Q. Liu, H. Yin, K. Mori, Y. Kuwahara, G. Li, T. An, H. Yamashit, Manipulation of plasmon-induced hot electron transport in Pd/MoO<sub>3-x</sub>@ZIF-8: boosting the activity of Pd-catalyzed nitroaromatic hydrogenation under visible-light irradiation, *Appl. Catal. B-Environ.* 282 (2021), 119511.

[54] Q. Wang, F. Fu, S. Yang, M. Martinez Moro, M. de los A. Ramirez, S. Moya, L. Salmon, J. Ruiz, D. Astruc, Dramatic synergy in CoPt nanocatalysts stabilized by “click” dendrimers for evolution of hydrogen from hydrolysis of ammonia borane, *ACS Catal.* 9 (2019) 1110–1119.

[55] F.H. Westheimer, The magnitude of the primary kinetic isotope effect for compounds of hydrogen and deuterium, *Chem. Rev.* 61 (1961) 265–273.

[56] M.T.M. Koper, R.A. van Santen, Interaction of H, O and OH with metal surfaces, *J. Electroanal. Chem.* 472 (1999) 126–136.

[57] A.P. Grosvenor, M.C. Biesinger, R.S.C. Smart, N.S. McIntyre, New interpretations of XPS spectra of nickel metal and oxides, *Surf. Sci.* 600 (2006) 1771–1779.

[58] D. Astruc, *Organometallic Chemistry and Catalysis*, Springer, 2007. Chapter 3.

[59] O.V. Ozerov, Oxidative addition of water to transition metal complexes, *Chem. Soc. Rev.* 38 (2009) 83–88.

[60] L. Luo, Z. Duan, H. Li, J. Kim, G. Henkelman, R.M. Crooks, Tunability of the adsorbate binding on bimetallic alloy nanoparticles for the optimization of catalytic hydrogenation, *J. Am. Chem. Soc.* 139 (2017) 5538–5546.

[61] S. García, L. Zhang, G.W. Piburn, G. Henkelman, S.M. Humphrey, Microwave synthesis of classically immiscible rhodium–silver and rhodium–gold alloy nanoparticles: highly active hydrogenation catalysts, *ACS Nano* 8 (2014) 11512–11521.

[62] P. Kunal, H. Li, B.L. Dewing, L. Zhang, K. Jarvis, G. Henkelman, S.M. Humphrey, Microwave-assisted synthesis of Pd<sub>x</sub>Au<sub>100-x</sub> alloy nanoparticles: a combined experimental and theoretical assessment of synthetic and compositional effects upon catalytic reactivity, *ACS Catal.* 6 (2016) 4882–4893.

[63] I.T. McCrum, M. Koper, The role of adsorbed hydroxide in hydrogen evolution reaction kinetics on modified platinum, *Nat. Energy* 5 (2020) 891–899.

[64] D.A. Dowden, 56. Heterogeneous catalysis. Part I. Theoretical basis, *J. Chem. Soc.* (1950) 242–265.

[65] M. Mavrikakis, B. Hammer, J.K. Nørskov, Effect of strain on the reactivity of metal surfaces, *Phys. Rev. Lett.* 81 (1998) 2819.

[66] V. Ponec, Alloy catalysts: the concepts, *Appl. Catal. A Gen.* 222 (2001) 31–45.

[67] J.K. Nørskov, T. Bligaard, J. Rossmeisl, C.H. Christensen, Towards the computational design of solid catalysts, *Nat. Chem.* 1 (2009) 37–46.

[68] C. Wei, Y. Sun, G.G. Scherer, A.C. Fisher, M. Sherburne, J.W. Ager, Z.J. Xu, Surface composition dependent ligand effect in tuning the activity of nickel–copper bimetallic electrocatalysts toward hydrogen evolution in alkaline, *J. Am. Chem. Soc.* 142 (2020) 7765–7775.